J. Fluid Mech. (2020), *vol.* 891, A1. © The Author(s), 2020.
Published by Cambridge University Press
doi:10.1017/jfm.2020.106

Time-resolved topology of turbulent boundary layer separation over the trailing edge of an airfoil

Austin Ma[1], **Bradley Gibeau**[1] and **Sina Ghaemi**[1,†]

[1]Department of Mechanical Engineering, University of Alberta, Edmonton, Alberta T6G 2R3, Canada

(Received 13 July 2019; revised 22 January 2020; accepted 2 February 2020)

The unsteady organization of a separated turbulent boundary layer was investigated upstream from the trailing edge of a NACA 4418 airfoil. The angle of attack was 9° in the pre-stall regime. Two particle image velocimetry fields of view were of interest: a streamwise–wall-normal plane at midspan of the airfoil and a streamwise–spanwise plane parallel to and near the surface of the airfoil. In the near-surface streamwise–spanwise plane, the mean velocity field revealed a saddle point near midspan and a pair of counter-rotating foci at the sides. This pattern is reminiscent of a stall cell, which has been traditionally associated with flow separation on thick airfoils at and slightly beyond the angle of attack of maximum lift. Isolating the low frequencies showed that the instantaneous separation front consisted of several smaller structures that also resembled a stall cell pattern, but they were an order of magnitude smaller than the one found in the mean pattern. These instantaneous stall cells were of two types: forward and backward. The forward stall cells were formed by strong high-speed streaks from upstream, while backward stall cells formed as a result of strong backflow just downstream from the separation front, resulting in a foci pair and a saddle point on their upstream side. In both cases, the foci pairs acted to mobilize high-speed momentum of the associated streak into a rotational motion, causing these streaks to dissipate. Finally, proper orthogonal decomposition revealed that low-order modes were associated with the movement and distortion of the separation front.

Key words: boundary layer separation, turbulent boundary layers

1. Introduction

The separation of a turbulent boundary layer due to an adverse pressure gradient (APG) is a phenomenon potentially observed in flow over airfoils, blades of a wind turbine, and within diffusers. In engineering applications, flow separation is typically linked to a decrease in the performance of the fluidic device. For example, a stalled airfoil generates significantly less lift and more drag than an airfoil operating under normal conditions. The unsteady nature of the airfoil wake due to separation can also introduce unwanted structural vibrations. In many applications that are prone to

---

[†] Email address for correspondence: ghaemi@ualberta.ca

flow separation, the peak performance of a device occurs at the brink of or soon after separation. This is a strong incentive for developing a thorough understanding of and predictive models for flow separation. Current analytical models cannot predict the unsteady behaviour of separation, and prediction using computational techniques is limited to relatively low Reynolds numbers (Na & Moin 1998; Jones, Sandberg & Sandham 2008) because the computations require tremendous amounts of computing power. Experimental results are therefore important for fundamental investigation, validation of numerical results, and for aiding the development of new analytical models.

There are two types of flow separation: flow detachment caused by an abrupt change of surface geometry and flow detachment from a relatively flat surface caused by an APG. The latter is referred to as APG-induced separation and was defined by Sears & Telionis (1975) as the departure of the boundary layer flow accompanied by a large wall-normal motion. A distinct feature of APG-induced separation is the intermittency of the separation due to the unsteadiness of the flow, as the location of separation moves back and forth on the surface (Simpson 1981). To characterize the intermittency of the separation region, researchers proposed the backflow parameter γ, which is defined as the fraction of time the flow is in the downstream direction (Simpson 1981). The backflow parameter can be used along with mean velocity fields to characterize flow separation. Even when the mean flow is considered, the separation point is strongly dependent on the Reynolds number and pressure gradient, and flow reattachment can occur at a downstream location depending on the strength of the APG (Alving & Fernholz 1996).

Similarly to many other areas of fluid mechanics, the investigation of flow separation began with the simplest case: two-dimensional flow. However, creating a fully two-dimensional separation in a wind tunnel proved to be difficult due to the interference of the sidewalls or other unknown interferences. For example, the flow over a stalled two-dimensional airfoil results in a three-dimensional separation (Moss & Murdin 1970; Gregory *et al.* 1971; Winkelman & Barlow 1980). Gregory *et al.* (1971) and Coles & Wadcock (1979) attempted to create two-dimensional flow separation by suction/blowing along the walls. Gregory *et al.* (1971) observed that suction along the wall removed corner separations, but three-dimensionality remained in the mean flow patterns. Coles & Wadcock (1979), Thompson & Whitelaw (1985) and Wadcock (1987) succeeded in forcing a two-dimensional flow through implementation of vanes/fences along the sidewalls. Confirmation of two-dimensional separation was mostly achieved through either surface oil flow visualization (SOFV) or wall pressure profiles. Both these techniques reveal little about the flow's unsteadiness, and the two-dimensionality was only confirmed for the mean flow. For this reason, it is difficult to say whether the separation in some of these studies was truly two-dimensional, as instantaneous spanwise motion could exist.

The importance of studying three-dimensional separation stems from the fact that flow in the practical world is rarely two-dimensional. In three-dimensional flow, the separation point is identified by a singular or critical point in the skin-friction pattern known as a saddle point (Tobak & Peake 1982). The other types of critical points, i.e. nodes and focus points, do not necessarily indicate flow separation. However, their arrangement specifies the skin-friction pattern, which can be used to provide insight on the topology of the separated flow. Historically, critical points and skin-friction patterns were measured with SOFV (Winkelman & Barlow 1980; Dell'Orso & Amitay 2018). This technique only produces mean flow patterns and reveals little about the flow's unsteadiness because of its long settling time (Lu 2010). Depardon *et al.* (2005) looked into the viability of using particle image velocimetry (PIV) in a plane parallel to and near the surface for measuring skin-friction patterns by comparing PIV at different heights with SOFV. They performed their investigation on geometry-induced flow separation around a wall-mounted cube and classified the differences between PIV and SOFV results into positional and structural discrepancies. Positional differences between critical point locations found via PIV and SOFV were present in all cases but minimized with decreased measurement height. Structural differences, i.e. when the topology found using PIV and SOFV do not agree, can be prevented by ensuring the measurement plane is located sufficiently close to the surface. It should be noted that even SOFV measurements may not be an accurate representation of the skin-friction topology near separation since pigments tend to accumulate in this region, thus impacting the flow dynamics (Squire *et al.* 1962; Depardon *et al.* 2005). In addition to being non-intrusive, the advantages of using PIV for measurement of skin-friction lines include access to quantitative data and instantaneous skin-friction fields, and an increase of both spatial and temporal resolution.

A variety of surface topology have been associated with flow separation depending on the Reynolds number, angle of attack, airfoil aspect ratio and thickness, type of laminar-turbulent transition, and surrounding boundary condition (Broeren & Bragg 2001; Liu, Woodiga & Ma 2011; Dell'Orso & Amitay 2018). A distinguished flow-separation pattern, which is also the focus of the present investigation, is an 'owl-faced' skin-friction pattern known as a stall cell. This pattern was first observed by Winkelman & Barlow (1980) and the counter-rotating swirls on the surface correspond to a saddle point and a pair of counter-rotating foci (Délery 2013). Stall cells have been observed on the suction side of thick airfoils that undergo a trailing-edge separation (Broeren & Bragg 2001) or leading-edge separation (Yon & Katz 1998) at the angle of attack of maximum lift and a few degrees beyond that into the post-stall regime (Yon & Katz 1998; Dell'Orso & Amitay 2018). However, there is also evidence of stall cells at angles of attack prior to that of the maximum lift. For an airfoil with 18 % thickness and maximum-lift angle of attack of 9°, tuft visualization of Manolesos, Papadakis & Voutsinas (2014) showed a stall cell pattern at angles of attack as low as 7°. This angle is in the nonlinear pre-stall section of the lift curve. Ragni & Ferreira (2016) also observed a stall cell on an NACA 64-418 airfoil at an angle of attack of 11° while the maximum-lift angle of attack was 15°.

For stall cells observed during post-stall, Winkelman & Barlow (1980) and Yon & Katz (1998) established that the number of cells present on a stalled airfoil increases with growing aspect ratio. The geometric properties of stall cells were investigated by Manolesos & Voutsinas (2014*a*) and Dell'Orso & Amitay (2018); they observed that the number and size of stall cells is also influenced by the angle of attack. As the angle of attack is increased, the distance between the two foci increases (Manolesos & Voutsinas 2014*a*) and eventually leads to the formation of a new stall cell (Dell'Orso & Amitay 2018). These studies focused on the spatial organization of the time-averaged pattern.

The three-dimensional topology of stall cells has only been briefly investigated. As a preliminary study to aid future experiments on wings at high angles of attack, Winkelman & Barlow (1980) created a tentative model of the three-dimensional topology for stall cell patterns. They hypothesized that the two foci were generated by a spanwise vortex that connects one focus to the other, which they called the loop vortex. They also suggested that a second spanwise vortex existed at the trailing edge that rotated in the opposite direction of the loop vortex. Based on this topology, Weihs & Katz (1983) created a theoretical model relating the number of stall cells to the aspect ratio of the wing. The model was developed based on the assumption that stall cells are vortex rings generated from the instability of spanwise vortices from the separated shear layer. After a brief period, Yon & Katz (1998) discovered the model suggested by Winkelman & Barlow (1980) was not consistent with their experimental data. Instead, they suggested that there are vortices that begin at the two foci in the wall-normal direction and extend downstream into the wake in the streamwise direction. This was later validated by Manolesos & Voutsinas (2014*b*) and Ragni & Ferreira (2016) through stereoscopic PIV. Two additional spanwise vortices were also observed by Manolesos & Voutsinas (2014*b*): one at the separation line and another at the trailing edge. The two spanwise vortices rotated in opposite directions relative to each other. There is some agreement on the three-dimensional topology of stall cells, but additional studies should be performed for confirmation.

Previous experimental studies conducted on stall cells were performed using fine tufts (Yon & Katz 1998), SOFV (Winkelman & Barlow 1980; Dell'Orso & Amitay 2018) or low frame-rate PIV (Manolesos & Voutsinas 2014*b*; Ragni & Ferreira 2016; Dell'Orso & Amitay 2018), which reveal limited information about time-resolved behaviour. As a result, little is known about the unsteadiness of stall cells and the motion of coherent structures present within the instantaneous velocity fields. Yon & Katz (1998) linked stall cells to the low frequency phenomenon observed by Zaman, Mckinzie & Rumsey (1989), which they attributed to a transition between a stalled and unstalled state. Duquesne, Maciel & Deschênes (2015) investigated the unsteadiness of flow separation in a turbine diffuser using two-dimensional PIV. Although no stall cell was reported for this geometry, the flow separation inside this diffuser is also created by an APG. By using a reduced-order model obtained through proper orthogonal decomposition (POD), they were able to filter out noise and small-scale structures in the skin-friction lines. Duquesne *et al.* (2015) observed that many saddle points and foci occupied the separation zone, and that the foci in the separation front are larger and more energetic than the turbulent vortices. However, more experiments are required to extend such an analysis of the unsteady flow organization to airfoil trailing-edge separation.

This investigation applies time-resolved PIV to study the unsteady topology of a trailing-edge separation formed on a thick airfoil in the nonlinear pre-stall regime. Near-wall PIV performed at the separation region is used to obtain an approximation of the instantaneous and mean skin-friction lines. The skin-friction patterns are investigated with the goal of providing insight into the connection between instantaneous flow structures and the stall cell pattern of the mean flow. A thick airfoil with a large chord is used in a wind tunnel to develop a turbulent boundary layer that undergoes separation close to the airfoil trailing-edge. The boundary layer at midspan is characterized and the results are compared with the previous literature including both two- and three-dimensional separations. The pattern of the mean flow is characterized and compared to past observations. Time-resolved PIV snapshots are then used to probe the instantaneous structure of the separation front. Finally, POD is applied to determine the most energetic motions in the near-wall plane.

2. Experimental set-up

An APG-induced separation was achieved near the trailing edge of an NACA 4418 airfoil at a moderate angle of attack. This particular profile was selected

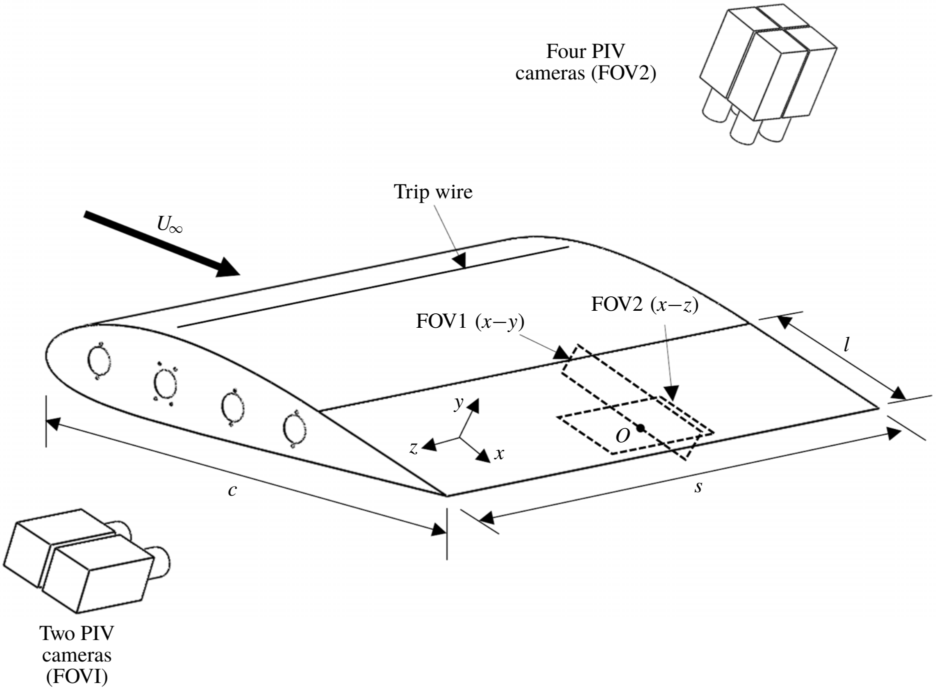

FIGURE 1. Schematic of the experimental set-up and PIV fields of view. The coordinates are defined relative to the flat surface of the airfoil. The origin of the coordinate system (O) is located at the separation point at midspan and 140 mm ($0.14c$) upstream of the trailing edge. Note that the axes are displaced from midspan of the airfoil for clarity of the figure.

because it features a gradual decrease of post-stall lift, which is typical for airfoils that experience trailing-edge stall (Abbott & Doenhoff 1959). Measurement of the separated flow was conducted using two separate planar PIV configurations. The two configurations are shown in figure 1, and additional details of the PIV set-ups are provided in §§ 2.2 and 2.3. The x-, y- and z-directions in this set-up are the streamwise, wall-normal and spanwise directions, respectively. The origin of the coordinate system (point O) is defined so that $x = 0$ is aligned with the mean separation point of the midspan plane, $y = 0$ is the surface of the airfoil, and $z = 0$ is midspan. The parameters U, V and W presented in this article are defined as the instantaneous velocity in the x-, y- and z-directions, respectively, while u, v and w are the fluctuating velocity components. The symbol $\langle \ldots \rangle$ represents the temporal average of the enclosed parameter.

2.1. *Wind tunnel and airfoil*

The experiments were performed inside a closed-loop wind tunnel at the University of Alberta with a $2.4 \times 1.2\ \mathrm{m}^2$ ($W \times H$) cross-section. A free stream speed of $U_\infty = 12\ \mathrm{m\ s^{-1}}$ was used for all experiments, resulting in a Reynolds number as defined by the airfoil chord length ($\rho U_\infty c/\mu$) of $Re_c = 750\,000$. The hotwire measurements of Gibeau & Ghaemi (2020) in this wind tunnel revealed a turbulence intensity of less than 0.5 % in the test section at the free stream speed considered. Transparent acrylic and glass walls allowed for conducting PIV experiments.

The NACA 4418 airfoil was constructed by folding an aluminium sheet around four equally spaced ribs. The ribs were machined using a water jet cutter to ensure a consistent profile. The airfoil has a chord length $c = 975$ mm and a span $s = 1200$ mm, corresponding to an aspect ratio of 1.2. A thick turbulent boundary layer was desired so that the turbulent motions could be spatially resolved with PIV, hence a large chord length was chosen. A 1 mm trip wire was placed on the upper surface at $0.2c$ to ensure uniform transition to turbulence along the span of the airfoil. In order to measure the near-surface flow with planar PIV, the NACA 4418 airfoil was customized to have a flat rear section of length $l = 350$ mm that extended from $0.67c$ to the trailing edge. The airfoil was mounted vertically inside the wind tunnel with no gap between the airfoil and the sidewalls.

An angle of attack of 9° was chosen through trial and error so that the mean separation point at midspan was located near the centre of flat trailing-edge section at $0.86c$. For the NACA 4418 airfoil, the slope of the lift curve begins to decrease at around 8°, signifying the start of trailing-edge separation (Abbott & Doenhoff 1959). With further increase of the angle of attack, the separation point gradually moves upstream and the positive slope of the lift curve reduces until the maximum lift is reached (McCullough & Gault 1951). The angle of attack corresponding to the maximum lift for this airfoil is approximately 14° at $Re_c = 3 \times 10^6$ (Abbott & Doenhoff 1959). In our preliminary investigations, we also observed that, by increasing the angle of attack, the separated region shifted in the upstream direction, i.e. from the trailing edge toward the leading edge. Therefore, the flow field of the current investigation, which includes trailing-edge separation at $0.86c$, is expected to be in the nonlinear pre-stall region prior to the angle of attack of maximum lift. Tuft visualization showed no leading-edge separation bubble upstream of the trailing-edge separation.

2.2. *Particle image velocimetry in the x–y plane*

The characteristics of the boundary layer at midspan were investigated using planar PIV at the field of view (FOV) labelled as FOV1 in figure 1. A fog generator was used to generate $\sim$1 μm droplets as flow tracers with a response time of $\sim$3 μs. The tracers in the FOV were illuminated using a dual-head Nd:YLF laser (Photonics Industries, DM20-527-DH), which is capable of outputting 527 nm light at maximum energy of 20 mJ per pulse with a pulse width of 170 ns. The laser was shaped into a sheet 1 mm thick using a combination of cylindrical and spherical lenses. Two coated mirrors were used to direct the laser sheet parallel to FOV1 along midspan. The illuminated tracers within the FOV were recorded using two high-speed cameras (Phantom v611) with a maximum resolution of 1280 pixel × 800 pixel. The cameras contain a complementary metal oxide semiconductor sensor with a 20×20 μm^2 pixel size. Greyscale images of the flow tracers were recorded at 12-bit depth. Both cameras were fitted with identical 105 mm Sigma lenses with aperture settings of $f/2$ and were placed 750 mm away from the viewing plane. At this distance, the fields of view of the cameras were 180×53 mm^2 and 181×53 mm^2, including a 15 mm overlap in the streamwise direction. The imaging system was calibrated to obtain the scaling and the relative orientation of the two fields of view by imaging a calibration grid. The image diameter of the tracer particles was approximately three pixels under this configuration.

Double-frame images were collected at 24 Hz with a delay of 150 μs between the laser pulses of adjacent frames. Five sets of images were collected, and each set of data contained 2700 images acquired over 112 s. Image and vector processing was performed using DaVis 8.4 (LaVision GmbH). In order to remove the background noise, the ensemble minimum was subtracted from all images. Normalization of the particle intensities was achieved by dividing the intensity values by the ensemble average. All images were cross-correlated multiple times with a final interrogation window size of 32 pixel $\times$ 32 pixel with 75 % overlap. The images were processed a second time using a sum-of-correlation algorithm (Meinhart, Wereley & Santiago 2000) with a final window size of 8 pixel $\times$ 8 pixel and 75 % overlap. The sum-of-correlation processing scheme allowed for smaller interrogation windows, resulting in a higher spatial resolution for the mean velocity field. This was desired for characterization of the boundary layer profile. Vectors with a normalized residual value of greater than 2 within a 3×3 vector window were considered to be outliers and removed (Westerweel & Scarano 2005). The number of outliers and empty vectors accounted for less than 0.5 % of the total vectors and were replaced by interpolation. The vectors from each camera FOV were stitched in DaVis based on the spatial coordinates obtained through calibration. After stitching the vector fields and removing the unwanted borders, the size of the effective FOV was $(\Delta x, \Delta y) = 325 \times 53\ \text{mm}^2$ with a digital resolution of 7.1 pixel mm^{-1}.

The measurements collected from this FOV are used to determine Reynold stresses and turbulence transport terms. Statistical convergence of these second- and third-order central moments was verified by plotting them against the number of samples at 50 locations distributed throughout the FOV. The difference between the maximum and minimum value for the last 20 % of each convergence curve was calculated. The random error of each parameter was estimated as the maximum difference from the 50 locations. The random errors of $\langle u^2 \rangle / U_\infty^2$, $\langle v^2 \rangle / U_\infty^2$ and $\langle uv \rangle / U_\infty^2$ are estimated to be 2.8, 0.6 and 1.1×10^{-4}, respectively. The random errors of $\langle u^3 \rangle / U_\infty^3$ and $\langle u^2 v \rangle / U_\infty^3$ are 11 and 2.5×10^{-5}, respectively.

2.3. *Particle image velocimetry in the x–z plane*

The near-surface flow in a plane parallel to the flat section of the airfoil was measured using planar PIV in the FOV denoted as FOV2 in figure 1. The same laser and Phantom v611 cameras used in the first configuration were also used in this set-up. A combination of spherical and cylindrical lenses was used to collimate the laser beam into a 1-mm-thick laser sheet, which was directed parallel with the surface of the model using a large mirror. The centre of the laser sheet was 2 mm away from the flat surface of the airfoil. Four cameras were used to increase the size of the viewing region while maintaining a large spatial resolution. Each camera was fitted with a 200-mm Nikon lens with an aperture setting of $f/4$ and extension rings. The front of the lens was positioned 1550 mm from the region of interest. Due to the physical size of the cameras, they were angled slightly in order to obtain a 15 mm overlap in the streamwise direction and 25 mm overlap in the spanwise direction. Because the angle was less than 1.0°, the parallax error introduced by tilting the cameras is less than 0.1 %. After stitching the images and removing the unwanted edges, the effective FOV was $(\Delta x, \Delta z) = 170 \times 230\ \text{mm}^2$ with a digital resolution of 7.9 pixel mm^{-1}. The image diameter of the tracer particles was visually determined to be approximately three pixels.

The sampling duration of each data set was limited by the storage capacity of the high-speed cameras. Consequently, two different camera settings were utilized for recording images within FOV2: one to obtain a large quantity of uncorrelated vector fields and another to gather time-resolved data. The uncorrelated data were collected in a cyclic multi-frame mode, in which each cycle consisted of five successive images at 1750 Hz. The cycles were acquired every second for a total duration of 60 s. The measurement was repeated 20 times to obtain 1200 uncorrelated cycles. By acquiring five images at a high temporal rate of 1750 Hz within each cycle, a sliding-average correlation could be used for the evaluation of the velocity vectors to increase the signal-to-noise ratio (Ghaemi, Ragni & Scarano 2012). The time-resolved data consisted of five sets of 5000 single-frame images at 1750 Hz. The uncorrelated images obtained from the first acquisition method will be referred to as the cyclic data while the latter will be referred to as the time-resolved data. The cyclic data were suitable for obtaining statistically converged quantities for some of the analyses including the evaluation of mean velocity field, Reynolds stresses, and POD. In contrast, the time-resolved data was used to gain insight into the evolution of coherent structures present in the separation region.

All image and vector processing was performed using DaVis 8.4 once again. Background noise was removed by subtracting the ensemble minimum and then normalization was achieved by dividing the intensity values by the ensemble average. All images were cross-correlated using a sliding sum-of-correlation of five successive frames (Ghaemi *et al.* 2012). The use of sliding sum-of-correlation reduced the number of incorrect and empty vectors. Multiple passes were used with a final interrogation window size of 48 pixel × 48 pixel and 75 % overlap. An outlier detection method, based on Westerweel & Scarano (2005), was applied to remove spurious vectors, which made up for less than 1 % of the total vectors and were replaced by interpolation.

2.4. *Detection and tracking of critical points*

The points on a surface where the wall shear, τ, is zero in all direction (i.e. $\tau_x = \tau_z = 0$) are known as the singular or critical points (Délery 2013). These critical points can be detected by identifying points with zero wall-normal gradient, i.e. $\mathrm{d}U/\mathrm{d}y = 0$, which along with the no-slip condition implies zero velocity in the immediate vicinity of the wall. However, since the measurements in the x–z plane were carried out at a wall-normal distance of $y = 2$ mm, a maximum threshold of 0.12 m s^{-1} ($0.01U_\infty$) was used for detecting the critical points. This threshold accommodates slight deviations from a linear $\mathrm{d}U/\mathrm{d}y$ profile. The threshold value was determined iteratively through visual inspection of the critical points relative to the streamlines. A threshold smaller than $0.01U_\infty$ did not detect all the critical points that could be identified by visualized inspection of the streamlines, and a threshold value greater than $0.01U_\infty$ resulted in the detection of several spurious critical points. Velocity magnitude is defined here as the magnitude of the two-dimensional velocity vector in the streamwise–spanwise plane only. The wall-normal velocity does not contribute to the shear stress at the wall. In the algorithm, duplication of critical points in a neighbourhood pertaining to the same structure were removed by only considering the local minima within a neighbourhood of 9 × 9 vectors (12 mm × 12 mm). After detection of the critical points, their classification is achieved by solving the equation introduced by Henri Poincaré (Délery 2013),

$$S^2 + pS + q = 0, \tag{2.1}$$

where

$$p = -\frac{\partial U}{\partial x} - \frac{\partial W}{\partial z}, \tag{2.2}$$

and

$$q = \frac{\partial U}{\partial x}\frac{\partial W}{\partial z} - \frac{\partial W}{\partial x}\frac{\partial U}{\partial z}. \tag{2.3}$$

The roots of (2.1), S, reveal the type of critical point present. Nodes exist when both roots are real and of the same sign, foci exist when the roots form a pair of complex conjugates, and saddle points are present when the roots are real with opposite signs. The partial derivatives of the velocity components on the right-side of (2.2) and (2.3) were computed by fitting the vectors with a least-squares-optimal quadratic using a kernel size of 5.

A simple tracking algorithm was developed to follow saddle points and foci in the time-resolved velocity fields. This was achieved by applying a $6 \times 6\ \text{mm}^2$ (5×5 vectors) tracking window to an identified saddle point/focus and searching for another saddle point/focus inside the window in the next two frames. If subsequent structures are found, then they are grouped and a track is generated. This procedure is repeated until no more structures can be detected inside the tracking window, in which case the track ends. This tracking window can follow structures that are advected by velocities up to $0.44U_\infty$ in the near-wall x–z plane. Tracks with a lifespan of less than 25 frames (0.014 s) were also removed to consider only the coherent motions with a longer lifetime and to eliminate noise. Finally, the tracks were smoothed using a kernel regression that implements a quadratic polynomial and a kernel size of 5.

3. Mean flow characteristics

In this section, the time-averaged statistics of the flow field, including mean velocity and Reynolds stresses, are analysed. The measurements in the streamwise–wall-normal plane at the midspan of the airfoil are compared with the literature on two- and three-dimensional separation, while the wall-parallel measurement plane is evaluated with respect to previous investigations of stall cells. All statistics in this section are obtained from the cyclic data to promote statistical convergence.

3.1. *Turbulent boundary layer*

The progression of the boundary layer profile with chordwise distance within FOV1 at midspan is shown in figure 2(*a*). Contours of the mean streamwise velocity are also shown in the background. The dashed line is located along $\langle U \rangle = 0$, with the positive contours located above and the negative contours located below. The streamwise coordinate was normalized by the chord length of the airfoil (c) and the wall-normal coordinate was normalized by the boundary layer thickness (δ_{99}) obtained at $x/c = -0.15$, which is 26.3 mm. The mean separation point is evident from the detachment of the boundary layer from the surface at $x/c = 0$, which is followed by a recirculation region with backflow.

The shape factor of the boundary layer (H, the ratio of displacement and momentum thicknesses) at $x/c = -0.15$ is 2.1, which is larger than the typical value of roughly 1.3 for a turbulent boundary layer with zero pressure gradient (ZPG) (Schlichting & Gersten 2016). As expected, this is because the boundary layer is subject to an APG, and the effect is evident even at the most upstream region of the FOV. A reduction of streamwise velocity and an increase of wall-normal velocity are observed with downstream distance. In table 1, the variation of both velocity components is shown for the farthest measurement data from the wall at $y = 2\delta_{99}$, which is indicated with ∞ and x subscripts for the specified streamwise position. The boundary layer

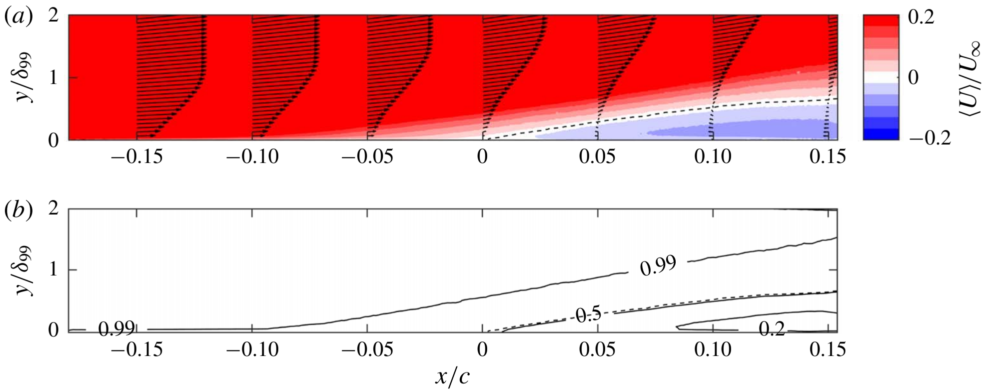

FIGURE 2. (*a*) Vectors of mean velocity at various chordwise positions upstream and downstream of the mean separation point ($x/c = 0$). The vector profiles are shown in $0.05c$ increments and the vectors are downsampled by a factor of 6 in the y-direction for clarity of the visualization. Contours of the normalized mean streamwise velocity, $\langle U\rangle/U_\infty$, are shown in the background. Positive contours are above the dashed line and negative contours are located under the dashed line. (*b*) Contour lines of the backflow parameter (γ) in the x–y plane. The dashed line indicates where the mean streamwise velocity is zero.

x/c	$U_{\infty,x}$ (m s^{-1})	$V_{\infty,x}$ (m s^{-1})	δ_{99} (mm)	δ^* (mm)	θ (mm)	H
−0.15	12.83	1.21	26.3	9.3	4.3	2.1
−0.10	12.33	1.30	31.5	12.6	5.1	2.5
−0.05	12.10	1.49	37.8	17.2	5.9	2.9
0.00	11.89	1.69	45.5	23.2	6.4	3.6

TABLE 1. Boundary layer parameters for various positions upstream of, and at mean separation.

thickness (δ_{99}), displacement thickness (δ^*), momentum thickness (θ) and shape factors (H) of the upstream boundary layer are also provided. The values are only provided up to $x/c = 0$ because the boundary layer thickness falls outside the FOV downstream of the mean separation point.

The effect of the APG can also be seen from the wall-normal velocity gradient ($\partial\langle U\rangle/\partial y$) of the velocity profile in figure 2(*a*). As the mean separation point is approached, the wall-normal velocity gradient of the boundary layer decreases and the velocity profile loses the fullness that is exhibited by a turbulent-boundary layer in ZPG. The change is highlighted by the increase of the shape factor with downstream distance. A value of $H = 3.6$ is reached at the mean separation point. This value is similar to the shape factors obtained by previous studies of two-dimensional separation performed by Wadcock (1987), Holm & Gustavsson (1999) and Angele & Muhammad-Klingmann (2006). A reduced shape factor of 2.85 was reported in the experiments conducted by Dengel & Fernholz (1990). The difference may be attributed to the fact that their investigations were performed over an axisymmetric body rather than a flat surface.

Contours of the backflow parameter (γ) are shown in figure 2(*b*). Once again, the line of zero mean streamwise velocity is shown by the dashed line in figure 2(*b*),

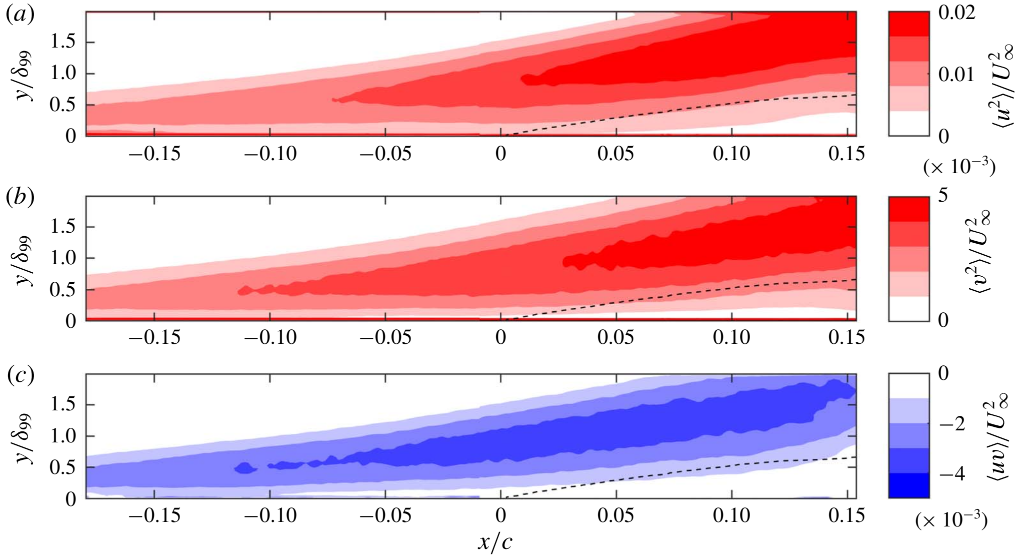

FIGURE 3. Contours of (*a*) streamwise (*b*) and wall-normal Reynolds stresses, and (*c*) Reynolds shear stress in the x–y plane. The dashed line shown in the figures indicates $\langle U\rangle = 0$. The values are normalized using the free stream speed of the wind tunnel U_∞.

which coincides with the contour line $\gamma = 0.50$. The contour line $\gamma = 0.50$ originates from a point on the surface known as the transitory detachment point (Simpson 1989) that is also close to the origin here. As expected, the probability of backflow increases with increasing downstream distance.

3.2. *Reynolds stresses and turbulence transport at midspan*

The normal and shear Reynolds stresses in the x–y plane are normalized by the free stream velocity and shown in figure 3. All three Reynolds stresses exhibit a similar trend: the local peak of the wall-normal profiles moves away from the wall with increasing streamwise distance. Previous researchers have also observed a similar distribution of the Reynolds stresses in a streamwise–wall-normal plane within two-dimensional (Thompson & Whitelaw 1985; Angele & Muhammad-Klingmann 2006) and three-dimensional separation (Manolesos & Voutsinas 2014*b*; Elyasi & Ghaemi 2019). These authors attributed the trend to the separation of the boundary layer and the roll up of vortices. The roll up of vortices due to separation also increases turbulence mixing in this region, as indicated by the high intensity region of the $\langle uv\rangle/U_\infty^2$ distribution in figure 3(*c*). Minimal shear stress is seen in the backflow region under the dashed line of $\langle U\rangle = 0$, which indicates negligible mixing inside the recirculation region.

The transport of streamwise turbulent kinetic energy due to streamwise and wall-normal fluctuations is evaluated using the third-order central moments, $\langle u^3\rangle/U_\infty^3$ and $\langle u^2v\rangle/U_\infty^3$, respectively. The results are shown using the contours of $\langle u^3\rangle/U_\infty^3$ and $\langle u^2v\rangle/U_\infty^3$ in figures 4(*a*) and 4(*b*), respectively. The distributions are similar to those obtained by Elyasi & Ghaemi (2019) from an APG-induced three-dimensional separation inside a diffuser. In the current investigation and in Elyasi & Ghaemi (2019), the flow is broken down into two layers: an outer region and an inner region.

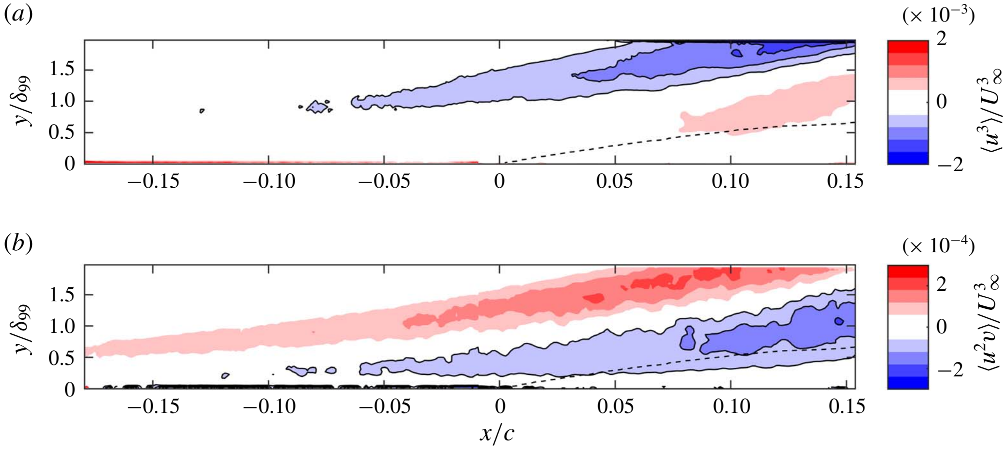

FIGURE 4. Contours of the third-order central moments (*a*) $\langle u^3\rangle/U_\infty^3$ and (*b*) $\langle u^2v\rangle/U_\infty^3$ in the x–y plane. The turbulence transport terms are normalized by the free stream speed of the wind tunnel U_∞. The dashed line shown in the figures indicates $\langle U\rangle=0$. Contours enclosed with solid lines denote negative values and contours without solid borders denote positive values.

The outer region contains negative $\langle u^3\rangle/U_\infty^3$ and positive $\langle u^2v\rangle/U_\infty^3$ and suggests that streamwise turbulent kinetic energy is transported away from the wall through ejection motions, i.e. negative u and positive v. In contrast, the inner region contains positive $\langle u^3\rangle/U_\infty^3$ and negative $\langle u^2v\rangle/U_\infty^3$, which indicates that streamwise turbulence is transported through sweeping motions, i.e. positive u and negative v.

Comparing the present results to those from past investigations reveals that there are similarities between different separated flows when the streamwise–wall-normal plane at midspan is viewed. For example, all two- and three-dimensional separations have shown that the boundary layer profile undergoes a similar transformation leading up to the mean separation point. Similar behaviour of the Reynolds stresses is also observed; the local peak stress moves away from the wall with the separation of the boundary layer, accompanied by an increase of the Reynolds stresses and broadening of the associated peaks with downstream distance. Increasing of the Reynolds stress and broadening of the peak was also observed for separated flow over a smooth contoured ramp (Song & Eaton 2002), backward-facing step (Scarano & Riethmuller 1999) and a flat plate with a trailing flap (Thompson & Whitelaw 1985). The results for the third-order central moments presented here are also in agreement with Elyasi & Ghaemi (2019). These similarities were observed despite the fact that the three-dimensional topologies of the flows were different. The agreement suggests that the separated boundary layer and the roll-up of the shear layer, which is the common feature between these flows, has a major contribution to the Reynolds stress and turbulence transport in the streamwise–wall-normal plane.

The mean velocity field in FOV2 displayed in figure 5(*a*) is used to gain insight into the near-wall topology in the vicinity of the separation front. The measurement plane is located at $y=2$ mm, equating to $0.08\delta_{99}$ where δ_{99} is the boundary layer thickness at the most upstream position in the FOV ($x/c=-0.15$). The near-wall streamlines obtained in this plane are expected to be similar to the skin-friction lines with minor positional discrepancies according to the investigation of

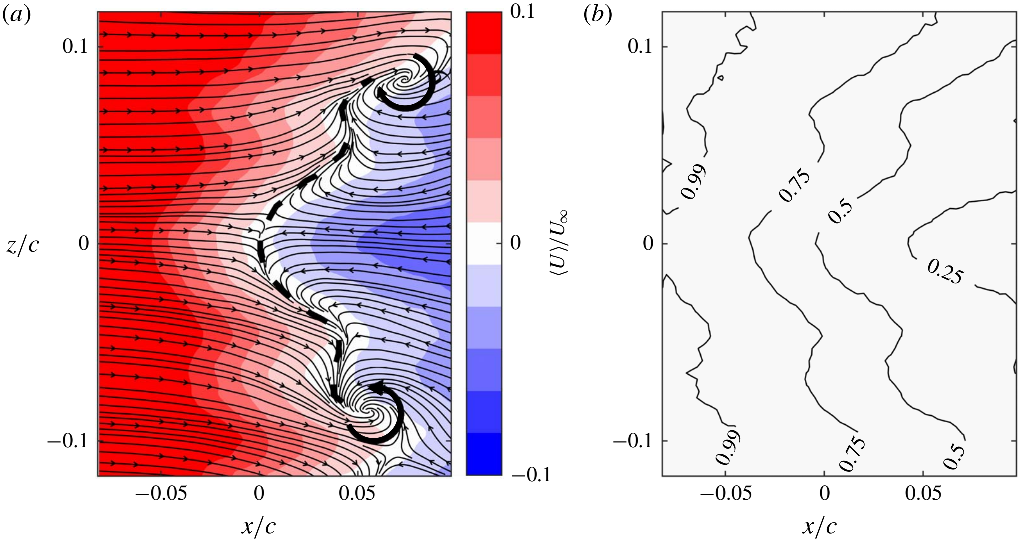

FIGURE 5. (*a*) Streamlines obtained from the mean flow in the near-surface ($y = 2$ mm) plane. Colours in the background represent the mean streamwise velocity normalized by free stream speed of the wind tunnel U_∞. The positive and negative contours can be identified based on the streamwise direction of the streamlines. (*b*) Contour lines of the backflow parameter (γ) in the near-surface plane, showing intermittency of the separated flow.

Depardon *et al.* (2005). They studied separated flow around a cube and observed topological consistency when the measurement plane is underneath the location of the main streamwise and spanwise vortical structures. For wall-normal vortices, the near-wall PIV measurements are not expected to deviate from the skin-friction topology except for minor positional discrepancies. In addition, this measurement plane is beneath the zone of maximum turbulence production. As was shown in figure 3, the zone of maximum Reynolds shear stress varies from $y/\delta_{99} = 0.5$ to 1.5 with increasing streamwise distance.

3.3. *Mean skin-friction lines*

The near-surface streamlines superimposed on the contours of streamwise velocity magnitude in figure 5(*a*) reveal a three-dimensional separation. A saddle point is present near midspan and a pair of counter-rotating foci are located at the sides, forming the stall-cell pattern. Such a stall cell pattern has been traditionally observed for thick airfoils at post-stall condition (Winkelman & Barlow 1980; Broeren & Bragg 2001; Manolesos & Voutsinas 2014*b*; Dell'Orso & Amitay 2018). However, Manolesos *et al.* (2014) and Ragni & Ferreira (2016) reported a stall cell for thick airfoils in the nonlinear pre-stall regime of the lift versus angle of attack curve. The detachment-type separation line, shown in figure 5(*a*) as a dashed line, rolls into the foci and forms tornado-like vortices. The separation line reveals an undulating pattern across the span. Spanwise motion is present at both spanwise sides of the saddle point immediately upstream of the separation line. This is explained by the tendency of flow to escape in the spanwise direction in the presence of an APG. In figure 5(*b*), the FOV captured most of the incipient detachment points ($\gamma = 0.99$) in the upstream

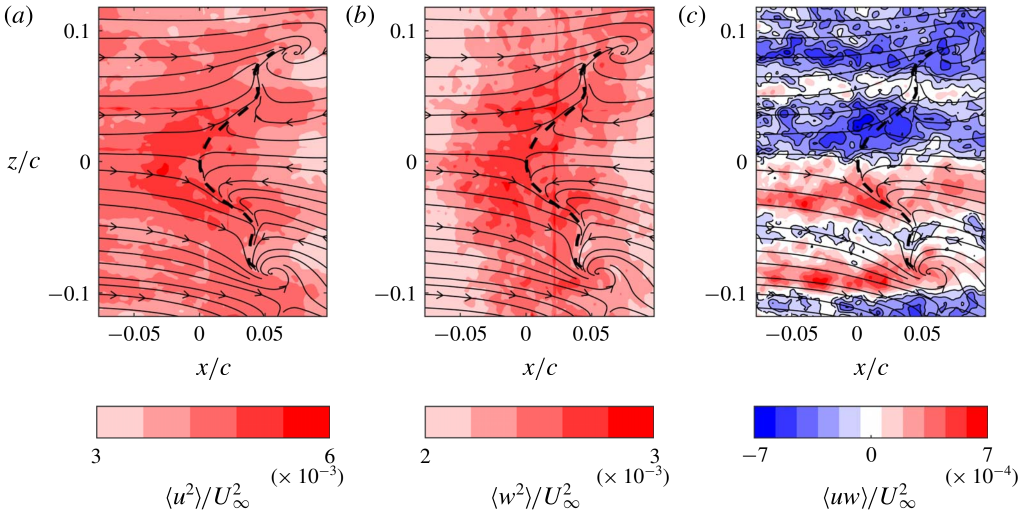

FIGURE 6. Contours of (*a*) streamwise and (*b*) spanwise components of Reynolds normal stress, and (*c*) Reynolds shear stress in the *x*–*z* plane. The near-surface streamlines obtained from the mean flow are superimposed on the contours. The negative contours are shown with solid black outlines.

region with the exception of the midspan region as shown by the contours of γ. It is noted that there are no points within the FOV where the flow is downstream ($U > 0$) or reversed ($U < 0$) at all instances, showcasing the intermittency of the flow and the large spatial influence of the present separation.

The distance between the two foci in the present study is approximately 0.17s (or 0.21c). Manolesos & Voutsinas (2014*a*) reported a minimum stall cell width of 0.25s for an airfoil with unspecified camber, an aspect ratio of 1.5, and Re_c of 1.5×10^6. Stall cell width in their investigation include the distance between the outer edges of the two foci, which means the distance between the two foci would have been less than 0.25s. They also applied zigzag tape over only 10 % of the span to stabilize the stall cell. Dell'Orso & Amitay (2018) observed a stall cell with an estimated distance of 0.18s between the two foci for Reynolds numbers between $Re_c = 4.0 \times 10^5$ and 4.5×10^5. Their study was conducted on a symmetric NACA 0015 airfoil with an aspect ratio of 4.0 and no trip wire was applied. It is also important to note that the stall cell observed by Dell'Orso & Amitay (2018) was in the post-stall regime while the smallest stall cell of Manolesos & Voutsinas (2014*a*) was observed for trailing-edge separation in the pre-stall regime. Considering the potential effects of angle of attack, airfoil profile, aspect ratio, type of laminar to turbulent transition, and Reynolds number, the size of the stall cell observed here is comparable to the observations of Manolesos & Voutsinas (2014*a*) and Dell'Orso & Amitay (2018).

3.4. *Reynolds stresses of the near-wall plane*

Reynolds stress contours in the near-wall *x*–*z* plane are presented in figure 6. Once again, the stress terms were normalized by the square of the free stream speed. The contours of $\langle u^2\rangle/U_\infty^2$ and $\langle w^2\rangle/U_\infty^2$ both reveal a symmetric pattern about midspan. By comparing the γ contours in figure 5(*b*) with the distribution of normal Reynolds stresses, it is evident that the largest $\langle u^2\rangle/U_\infty^2$ and $\langle w^2\rangle/U_\infty^2$ exist just upstream of where the separation line is most likely to be located (i.e. $\gamma \approx 0.50$). The increased fluctuation of both streamwise and spanwise velocity in this region indicates the large turbulence and intermittency of the flow structures that are present at the separation front. Downstream of the mean separation line, both $\langle u^2\rangle/U_\infty^2$ and $\langle w^2\rangle/U_\infty^2$ begin to decrease as the shear layer detaches from the surface and departs from the x–z plane of PIV. This agrees with the stress contours in the streamwise–wall-normal plane (figure 3), which show little mixing in the vicinity of the wall within the recirculation region.

The contours of the Reynolds shear stress shown in figure 6(*c*) are different from the contours of the normal stresses, as large magnitudes of shear stress appear in streamwise-elongated streaks. The streaks of large $\langle uw\rangle/U_\infty^2$ near $z/c = \pm 0.03$ are located along the detachment lines emanating from the saddle point of the mean flow. The secondary regions of large $\langle uw\rangle$ at $z/c = \pm 0.08$ are located at the same spanwise position as the two counter-rotating foci. There is also a deficit region of $\langle uw\rangle/U_\infty^2$, which is also elongated in the streamwise direction, and overlaps with the undulating part of the separation line at $z/c = \pm 0.05$.

4. Unsteady flow characteristics

The unsteady organization of the stall cell is investigated here by an initial evaluation of the energy spectrum of velocity fluctuations. Once the frequency range that forms the bulk of the turbulent kinetic energy is identified based on the spectrum, a low-pass filter is used to isolate the coherent motions. The filtered vector fields are also used to investigate the organization of the critical points and formation mechanism of the stall cell. Afterwards, the relationship between high-speed streaks and instantaneous separation structures is developed by comparing their spatial organizations.

4.1. *Energy spectra*

A discrete Fourier transform (DFT) was performed on the fluctuating velocity components obtained from the time-resolved images in FOV2 to identify the energy spectrum of the frequencies present in the flow. Welch's method was used to reduce spectral variance by performing DFT over overlapping segments and then averaging the results (Heinzel, Rüdiger & Schilling 2002). Hanning windows with 50 % overlap were applied to the segments to achieve amplitude flatness among all data points (Heinzel *et al.* 2002). A segment length of 0.50 s (874 images) was used, resulting in a frequency resolution of 2.0 Hz. The spectral density was evaluated for each set of time-resolved data (2.86 s) and then averaged (five sets in total).

The power spectral density (PSD) of the fluctuating streamwise velocity is presented in figure 7(*a*) and the PSD of the fluctuating spanwise velocity is shown in figure 7(*b*). Three points of interest along the midspan ($z = 0$) were selected: one upstream of the mean separation ($x/c = -0.05$), one at the saddle point ($x/c = 0$) and another within the region of reverse flow ($x/c = 0.05$). The three points were selected to determine the change of the frequency spectrum with increasing probability of backflow (i.e. decreasing γ). Spectral analysis of the fluctuating velocities at locations away from midspan were also investigated and yielded similar results.

As is evident in the plots of figure 7, the low-frequency fluctuations have a large kinetic energy at all three points. The energy of the velocity fluctuations decreases sharply with increasing frequency. No strong local peak is observed in the PSDs, indicating the absence of a strong periodic shedding process. At the low frequency range, the streamwise PSDs show a similar energy for all three points. However, at

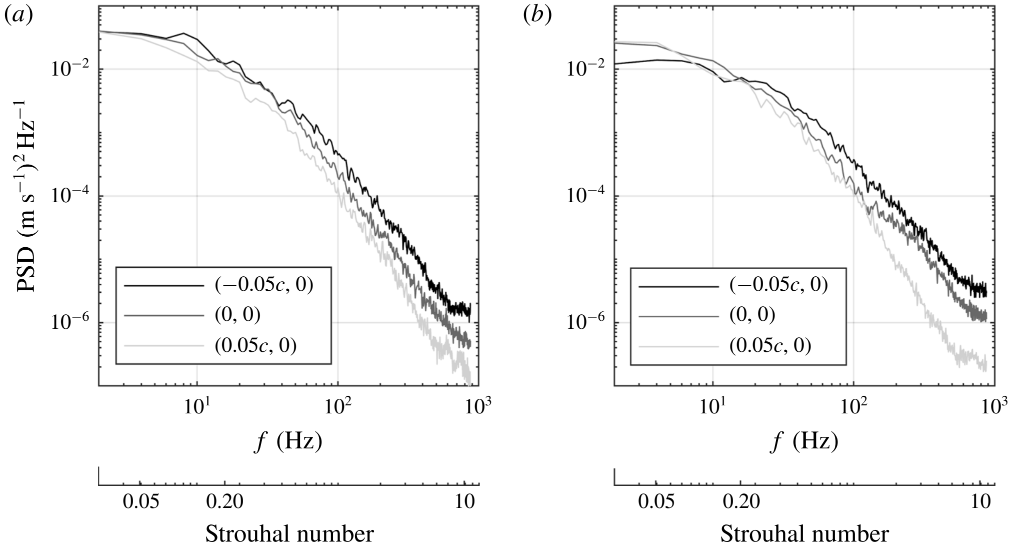

FIGURE 7. Power spectral density of the fluctuating (*a*) streamwise and (*b*) spanwise velocity at a location upstream of the mean separation point ($x/c=-0.05$), at the saddle point ($x/c=0$), and a point in the backflow region ($x/c=0.05$) along midspan ($z=0$).

higher frequencies, the energy reduces with streamwise distance. Since the backflow parameter also decreases with streamwise distance, the reduced high-frequency energy coincides with a larger probability of backflow motions.

Considering spanwise velocity fluctuations in figure 7(*b*), the low-frequency energy is smaller at the upstream point than it is at mean separation and within the backflow region. Investigation of the data at spanwise locations of $z/c=\pm 0.05$ and ± 0.10 also revealed smaller energy of low-frequency content at locations upstream of the mean separation line. The PSD at $z/c=\pm 0.05$ and ± 0.10 are excluded for brevity. At higher frequencies, the energy at the upstream points is larger. This trend indicates the presence of strong low-frequency spanwise motions at the separation point and its downstream locations (i.e. regions where $\gamma \leqslant 0.50$) as the flow turns in the spanwise direction in response to the APG. The presence of the spanwise motions was evident in the mean flow of figure 5(*a*) and $\langle w^2 \rangle$ contours of figure 6(*c*).

Zaman *et al.* (1989) conducted a study on the oscillation of flow around a stalled airfoil and concluded that bluff body vortex shedding appeared during deep stall at high angles of attack with a Strouhal number of 0.2. The Strouhal number was evaluated by normalizing the frequency, f, by the projected height of the airfoil and the free stream speed ($St=fc\sin\alpha/U_\infty$). At lower angle of attack, the vortex shedding frequency was replaced with a Strouhal number in the range of 0.02–0.05, which was associated with a shallow stall due to trailing-edge separation. A similar low-frequency phenomenon was observed by Yon & Katz (1998) for stalled airfoils that showed stall cell pattern. Zaman *et al.* (1989) attributed this low-frequency fluctuation to the transition of flow between a stalled and unstalled state. The second horizontal axis of figure 7 shows St, estimated using $fc\sin\alpha/U_\infty$. Most frequency content contained within the flow appears to be less than the bluff body shedding frequency of $St=0.20$. This agrees with the intermittency of trailing-edge separation as it is constantly alternating between forward and reverse flow, i.e. separated and attached.

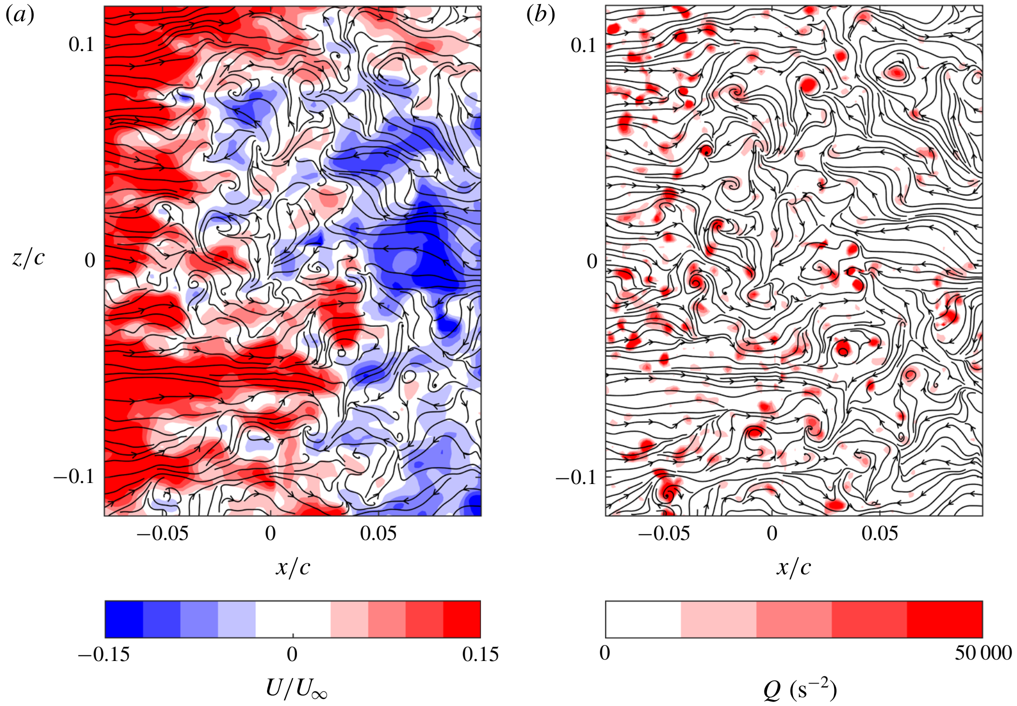

FIGURE 8. Snapshot of the instantaneous near-surface streamlines with a background contour of (*a*) normalized streamwise velocity and (*b*) two-dimensional Q-criterion. The sign of the contours in (*a*) can be identified using the streamwise direction of the streamlines.

4.2. *Spatial organization of critical points*

A sample snapshot of the instantaneous skin-friction lines is presented in figure 8(*a*) along with background contours of the normalized instantaneous streamwise velocity (U/U_∞). This figure provides a glimpse of the complicated nature of the flow field under investigation. The relatively parallel skin-friction at the upstream boarder of the FOV becomes chaotic as the flow evolves from an attached boundary layer to a separated flow with patches of backflow. The instantaneous separation line is not well defined in the visualization. Saddle points, foci and nodes can be observed throughout. These structures are intertwined with each other and the small-scale turbulence, making it hard to isolate individual structures. There is also no distinct resemblance of a stall cell in this instantaneous visualization. In figure 8(*b*), background contours of two-dimensional Q-criterion (Jeong & Hussain 1995) are used to show vortices with strong local rotation within the FOV. Although several patches of large Q are observed, no distinct pair of counter-rotating vortices is observed to guide us toward identifying a stall cell pattern.

In order to remove the small-scale, high-frequency structures from the instantaneous snapshots, a moving average filter is applied to the time-resolved data. The filter is used to isolate the low-frequency motion shown in the spectral analysis of figure 7 and observed in past studies (Zaman *et al.* 1989; Yon & Katz 1998). The moving average filter acts as a low-pass filter with a −3 dB cutoff frequency at $St = 0.05$, which was chosen based on the values provided by Zaman *et al.* (1989). They stated

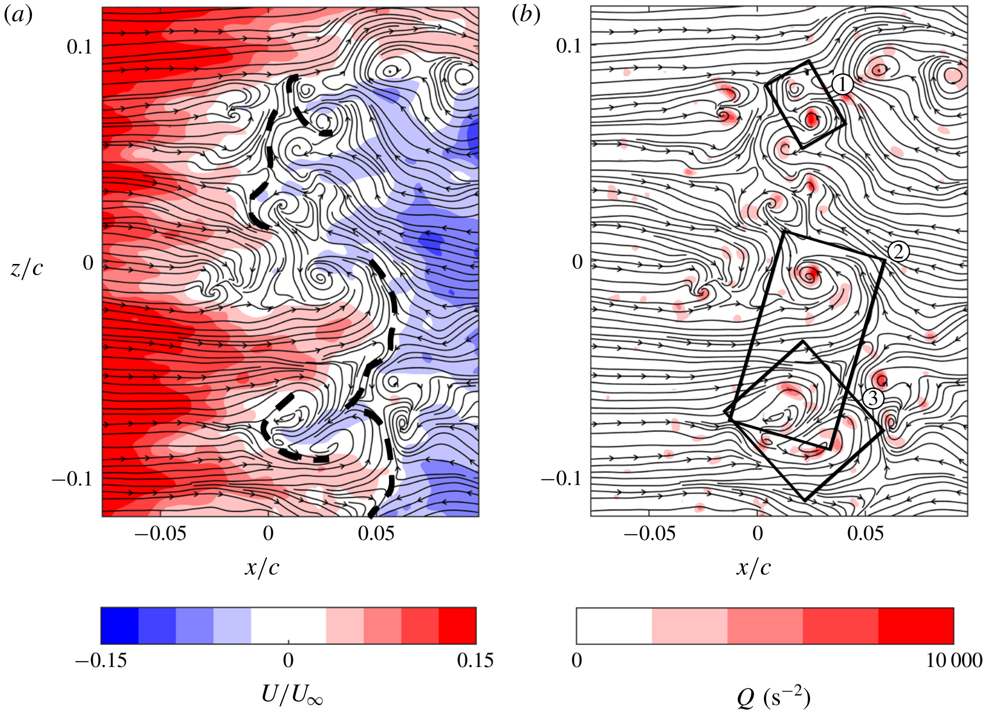

FIGURE 9. Filtered streamlines of the instantaneous velocity field in figure 8 with (*a*) instantaneous streamwise velocity and (*b*) two-dimensional Q-criterion shown in the background. A moving average filter with cutoff frequency at $St = 0.05$ was applied. Once again, the colour of the contours in (*a*) can be identified through the streamwise direction of the streamlines. Rectangles 1 and 3 in (*b*) show backward stall cells, while rectangle 2 shows a forward stall cell.

that the low frequency motions associated with a mild stall have a non-dimensional frequency between $St = 0.02$ and 0.05. Yon & Katz (1998) later connected this low frequency motion to airfoils with stall cell pattern. This cutoff frequency corresponds to a kernel size of $k = 200$ snapshots for the image acquisition frequency of 1750 Hz, which spans over 0.114 s. The instantaneous snapshot of figure 8 has been filtered as described above and is shown in figure 9(*a*) with normalized instantaneous velocity and in figure 9(*b*) with Q-criterion in the background.

At a first glance of the skin-friction lines in figure 9, it is observed that the majority of the small turbulent vortices with a shorter life-time have been removed from the snapshot due to filtering. The separation structures also appear to be more identifiable through visual inspection. The separation front is three-dimensional and made up of many local separation lines forming from small-scale saddle points. A few of these local separation lines are shown by the dashed lines in figure 9(*a*). All these separation lines pass through a saddle point and the neighbouring skin-friction lines converge as they approach the separation line. However, even after application of the filter, there is no distinct separation line that extends across the entire spanwise length of the FOV as seen in the mean flow of figure 5(*a*).

According to Surana, Grunberg & Haller (2006), the separation line emanating from a saddle point must terminate at either a node or focus, which is true for the instantaneous skin-friction lines shown in figure 9. The local separation lines

Advection velocity ($\times 10^{-4}$)	Saddle points	CW foci	CCW foci
$\langle U_a \rangle / U_\infty$	31 ± 2.1	38 ± 2.5	35 ± 1.7
$\langle \lvert U_a \rvert \rangle / U_\infty$	144 ± 1.7	135 ± 3.1	130 ± 1.0
$\langle W_a \rangle / U_\infty$	-3 ± 1.5	2 ± 1.2	-10 ± 3.6
$\langle \lvert W_a \rvert \rangle / U_\infty$	113 ± 1.2	88 ± 3.7	89 ± 1.0

TABLE 2. Advection velocities and speed of saddle points and foci evaluated based on the tracks detected in five sets of filtered time-resolved data.

sometimes terminate in a pair of counter-rotating foci as identified by the three rectangular boxes in figure 9(*b*), resulting in 'instantaneous stall cells' that are smaller than the stall cell in the mean skin-friction pattern. It is also possible for two separation lines to terminate at the same focus as highlighted by the overlap of the instantaneous stall cells identified by boxes 2 and 3 in figure 9(*b*). By inspecting the visualizations, the width of these instantaneous stall cells (i.e. distance between the two foci) can range from $0.02s$ to $0.06s$ ($0.02c$–$0.07c$), which is an order of magnitude smaller than the width of the mean stall cell.

Further inspection of figure 9 shows two types of stall cell in this instantaneous visualization based on the flow direction between the foci pair and the relative location of the saddle point. There are local stall cells with a strong backward flow motion such as the ones identified in rectangles 1 and 3. The saddle point of these stall cells is pushed to the upstream side of the foci pair. The second type of stall cell consists of a strong inrush of forward flow as shown in rectangle 2. As a result, the saddle point is observed on the downstream side of the foci. Based on the direction of the flow between the foci pair, these two structures will be referred to as backward and forward stall cells, respectively.

The above analysis was repeated using a low-pass filter with different cutoff frequencies, which varied from $St = 0.02$ to 0.2. In general, the number of critical points increased with increasing cutoff frequency due to the appearance of a larger number of small-scale structures. At the highest cutoff frequency of $St = 0.2$, the organization of instantaneous stall cells became intertwined with small-scale structures, thus making the instantaneous structures less apparent. For the lowest cutoff of $St = 0.02$, it appeared that the instantaneous stall cells were partially filtered. However, the small instantaneous stall cells were present in all cases.

The low-pass filtered velocity fields from FOV2 have also been used to detect the critical points and track them in time using the algorithm described in § 2.4. A visualization of the trajectories of saddle points, clockwise (CW) foci, and counter-clockwise (CCW) foci based on 1.0 s of time-resolved data are shown in figure 10(*a*). The left-side axes of the plot show the x and z coordinates of the critical points while the horizontal axis shows time. The figure indicates that the translations of the critical points in the x and z directions are small since most of the tracks appear as relatively straight lines. The average streamwise advection velocity, $\langle U_a \rangle$, and the average streamwise advection speed, $\langle \lvert U_a \rvert \rangle$, for saddle points and foci were calculated from the detected tracks and are shown in table 2. The same calculation is also carried out for the average spanwise advection velocity, $\langle W_a \rangle$, and its speed, $\langle \lvert W_a \rvert \rangle$. Here, the absolute operator, $\lvert \ldots \rvert$, is applied to isolate the effect of the direction. All five sets of filtered time-resolved datasets were considered to obtain the values shown in table 2. Statistical convergence of the advection velocities

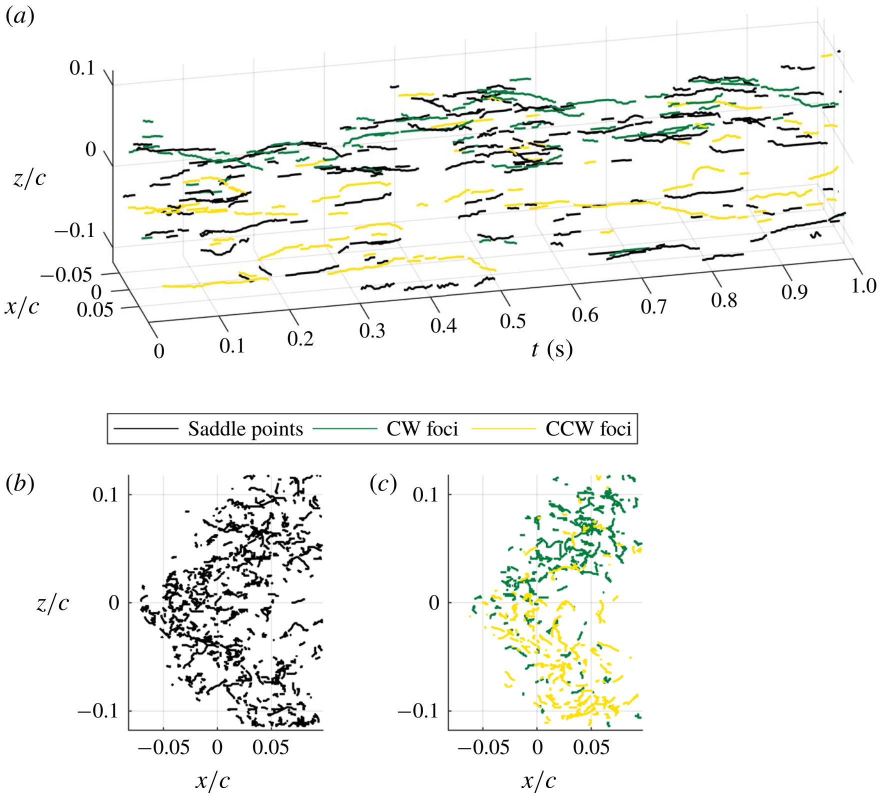

FIGURE 10. (*a*) Visualization of the detected tracks of saddle points, clockwise foci, and counter-clockwise foci over 1.0 s. Saddle points, clockwise foci, and counter-clockwise foci are shown with black, medium grey (green) and light grey (yellow) tracks, respectively. Tracks shown in the figures have a minimum length of 25 frames (0.014 s). The lower two plots show projections of the locations of the (*b*) saddle points and (*c*) foci obtained from 2.5 s of time-resolved data onto the *x*–*z* plane.

was verified by plotting the parameter against the number of sample points used for its calculation. The convergence tests showed that the values have statistically converged to their mean values. The random error of the values presented in table 2 were determined by finding the difference between the maximum and minimum value (the range) for the trailing 20 % of the convergence curve.

Advection of the saddle and focus points is observed in both the streamwise and spanwise directions as they both possess finite $\langle |U_a| \rangle$ and $\langle |W_a| \rangle$ values. The sign of $\langle U_a \rangle$ is positive for saddle and focus points, revealing that, on average, these structures tend to move in the downstream direction. However, the larger value of $\langle |U_a| \rangle$ with respect to $\langle U_a \rangle$ indicates that there is also a significant amount of backward advection in the upstream direction. Since saddle points and foci form along the separation lines of the instantaneous stall cells, the advection of these critical points is associated with movement and intermittency of the separation lines. Consequently, the separation lines are also expected to move in both the upstream and downstream directions with a slight tendency towards the downstream direction. The spanwise advection speed of the structures is also comparable with their streamwise speed. However, there is no spanwise preference as the average spanwise advection, $\langle W_a \rangle$, is negligible.

The tracks of saddle points and foci have been projected onto the x–z plane and presented in figures 10(b) and 10(c), respectively. These figures visualize the motion of the critical points in the x–z plane and approximate their probability density distributions. In both figures, the locations of the critical points form a V-shape distribution, similar to the pattern of the mean stall cell. The saddle points in figure 10(b) are evenly distributed between both halves of the span. In figure 10(c), the tracks of clockwise foci are shown in dark grey (green) while the tracks of counter-clockwise foci are shown in light grey (yellow). It is evident that the counter-clockwise foci are localized at the bottom of the FOV, while foci with clockwise rotation are centralized at the top. This preferential concentration of the foci structures is believed to form the foci pair of the mean stall cell pattern that was observed in figure 5(a), i.e. the average of counter-clockwise foci located at the bottom of the FOV forms the large mean counter-clockwise focus in the mean-velocity field, and vice versa for the clockwise focus that appears at the top of the FOV.

4.3. *Instantaneous forward and backward stall cells*

Inspection of the time-resolved skin-friction lines in movie 1 of the supplementary material available at https://doi.org/10.1017/jfm.2020.106 shows that foci pairs tend to form near regions of strong local flow at the separation front. This local flow results in high shear and the formation of counter-rotating, tornado-like vortices (the foci pair). In one presently observed scenario, the strong local flow originates from an influx of streamwise momentum from upstream flow in the form of a single high-speed streak. The high-momentum flow pierces an already existing separation front and forms the foci pair. The resultant skin-friction pattern is a saddle point with a pair of counter-rotating foci, i.e. an instantaneous stall cell. The motion corresponding to this topology is separation via a pair of tornado-like vortices (Délery 2013). As shown in the visualization of figure 9, these instantaneous stall cells can exist with either forward or backward orientations. In contrast to the above description, the latter forms as a result of a strong backflow from the downstream side of the separation front. By identifying the instantaneous stall cells as a pair of tornado-like vortices (Délery 2013), it is hypothesized that streamwise momentum is converted into wall-normal momentum during the formation of these structures.

The instantaneous stall cell formation described above is visualized in figure 11. Figure 11(a–d) show the formation of a forward stall cell due to a strong downstream flow, while figure 11(e,f) show the formation of a backward stall cell due to a strong backflow. The process is demonstrated through carefully selected timestamps here, but videos of the processes are provided in movies 2 and 3 of the supplementary material. Once again, these streamlines were obtained from the filtered data described in § 4.2. The subfigures contain a zoomed-in view of the structures with normalized instantaneous streamwise velocity (U/U_∞) plotted in the background of the streamlines. The separation lines of nearby saddle points are represented by dashed lines to highlight the movement of the instantaneous separation line.

Figure 11(a) reveals the skin-friction lines before the influx of streamwise momentum. The dashed lines in the subfigure are clearly separation lines because neighbouring skin-friction lines converge towards it. The local separation line on the left comes from a saddle point that is outside of the cropped FOV. After 0.055 s, a pair of foci is formed due to an inrush of strong streamwise flow as indicated by the arrow in figure 11(b). The centres of the two foci are located at approximately $(x/c,\ z/c) = (0,\ 0)$ and $(0.01,\ -0.03)$ in the figure. The two foci indicate that the

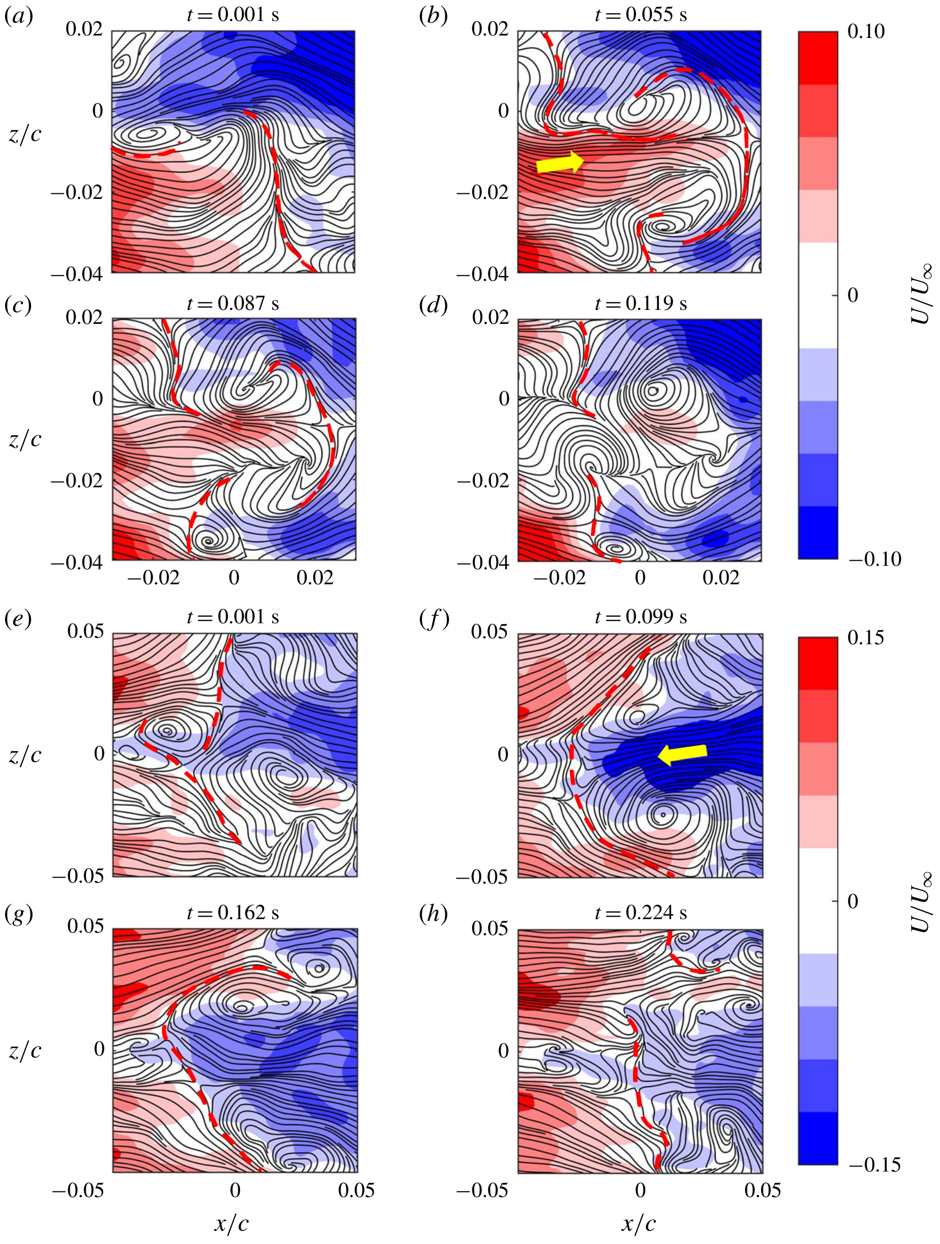

FIGURE 11. The formation and dissipation of (*a*–*d*) a forward stall cell and (*e*–*h*) a backward stall cell due to local concentrations of strong streamwise momentum. The colours in the background correspond to the normalized streamwise velocity. Videos of the process are provided in movies 2 and 3 of the supplementary materials online.

local flow ejects from the surface via a pair of tornado-like vortices that contain both spanwise and wall-normal momentum. As the incoming momentum subsides (figure 11*c*), the pair of foci eventually disintegrates and smaller, unstable structures are left behind as shown in figure 11(*d*). The formation process of a backward stall cell is the same but is spatially reversed as can be seen in figure 11(*e*–*h*). The strong backflow seen in figure 11(*f*) results in a pair of foci located at $(x/c, z/c) = (0, 0.01)$ and $(0.01, -0.03)$.

4.4. *High-speed streaks*

In § 4.3, it was evident that foci are located at high-shear regions of forward or backward flow at the separation front. One possible scenario is that these high-shear regions are created by an inrush of streamwise momentum from upstream high-speed streaks of the turbulent boundary layer. If this is the case, then the width of instantaneous stall cells should be similar to the spanwise spacing between high-speed streaks. In this section, the spanwise distance between adjacent high-speed streaks (λ_z) in the upstream turbulent boundary layer is evaluated through spatial autocorrelation of the streamwise fluctuating velocity in the spanwise direction, which is then compared with the size of instantaneous stall cells determined previously. The normalized correlation coefficient, which is determined using

$$\rho(\Delta z) = \frac{\langle u(x_i, z, t_n) \cdot u(x_i, z + \Delta z, t_n)\rangle}{u_{rms}(x_i, z, t_n)^2}, \tag{4.1}$$

can be a value between -1 and $+1$. The correlation curve is calculated for the nth snapshot at a specified streamwise position x_i. At zero shift ($\Delta z = 0$), the signal aligns perfectly and return a value of $\rho = 1$. As the signal is shifted, the correlation coefficient decreases until a local minimum value is reached. At this minimum, the signal has been shifted by half the spanwise wavelength of the streamwise fluctuations and can therefore be used to determine the associated wavelength. The autocorrelation function was applied to the cyclic data set for faster statistical convergence. Histograms of the spanwise wavelengths have been generated and a log-normal distribution was used to model the probability density function (p.d.f.) of the results.

The p.d.f.s of the spanwise wavelengths are plotted for three different chordwise positions in figure 12 to investigate the effect of chordwise position on streak width. The spanwise wavelengths of the streaks presented here are normalized by the span. The chordwise positions chosen correspond to an upstream location ($x/c = -0.05$), the mean separation point ($x/c = 0$) and a downstream location ($x/c = 0.05$). All three distributions are unimodal and are right-skewed to varying degrees. The upstream ($x/c = -0.05$) distribution features a peak located at $\lambda_z/s = 0.030$. In § 4.2, it was found that the width of instantaneous stall cells can range from approximately $0.02s$–$0.06s$. The p.d.f. corresponding to $x/c = -0.05$ reveals that a large majority of the upstream streak widths fall within this range. Consequently, the size of the instantaneous stall cells likely scales with the spacing between upstream high-speed streaks.

As the flow progresses downstream, the peak of the distribution moves to the right while the distribution broadens. At $x/c = 0$ and 0.05, the peak is shifted to $\lambda_z/s = 0.034$ and 0.044, respectively. Both of these peak locations (i.e. the most probable values) also fall within the aforementioned range of instantaneous stall cell sizes. The p.d.f. at the downstream location ($x/c = 0.05$) is quite broad, indicating that the size of the streaks varies considerably post separation. This is quantified by the standard deviation of the distribution, which increases from 0.011 to 0.022 between $x/c = -0.05$ and 0.05. The change in the p.d.f.s reinforces the notion that streaks evolve into two foci and a saddle structure at separation. As the streaks vanish from the

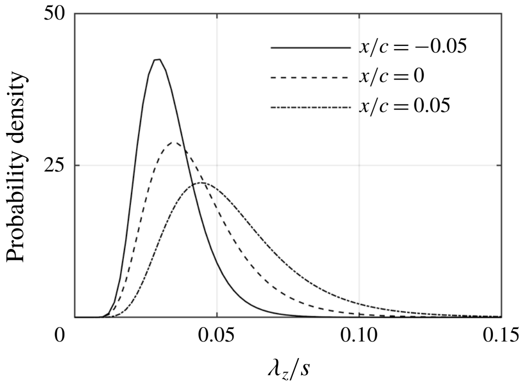

FIGURE 12. Probability density functions of the spanwise wavelength of high-speed streaks (λ_z/s) at three different chordwise positions. The wavelengths were determined by spatial autocorrelation of the fluctuating streamwise velocity using (4.1) and were fitted with a log-normal distribution.

measurement plane, the spacing between the streaks increases and λ_z will tend towards a larger value.

The evolution of the high-speed streaks moving through the measurement plane is shown using three-dimensional isosurfaces in figure 13(*a*). These isosurfaces have also been projected onto the x–t axis in figure 13(*b*) to highlight the advection of streaks in the streamwise direction. The streaks shown in the figure correspond to a segment of the unfiltered time-resolved data. There are a large number of high-speed streaks in the upstream region ($x/c < 0$) and a significant number of the streaks subside before they reach the downstream section of the FOV. This agrees with the p.d.f.s in figure 12 and further supports the notion that streamwise momentum from high-speed streaks forms separation structures once they reach the separation front instead of persisting downstream.

5. Energetic motions

In this section, the energetic motions of the near-wall flow are investigated via POD of the cyclic datasets. The motion attributed to the energetic modes are determined by adding the spatial mode onto the mean velocity field and then analysing the change.

Proper orthogonal decomposition by the method of snapshots (Sirovich 1987) was used to decompose the near-surface flow into a linear combination of optimal bases (POD modes). The instantaneous fluctuating velocity was used to obtain M spatial modes ($\boldsymbol{\phi}_m$), where M is the total number of snapshots used in the analysis. The modes are ordered based on energy content, with mode 1 containing the highest proportion of energy and mode M containing the least. The temporal amplitudes $a_m(t)$ represent the contribution of the corresponding mode m at time t. The data decomposition is mathematically represented by the equation

$$\boldsymbol{u}(x, z, t) = \sum_{m=1}^{M} a_m(t)\boldsymbol{\phi}_m(x, z). \tag{5.1}$$

The bolded notation indicates a vector in the x–z plane.

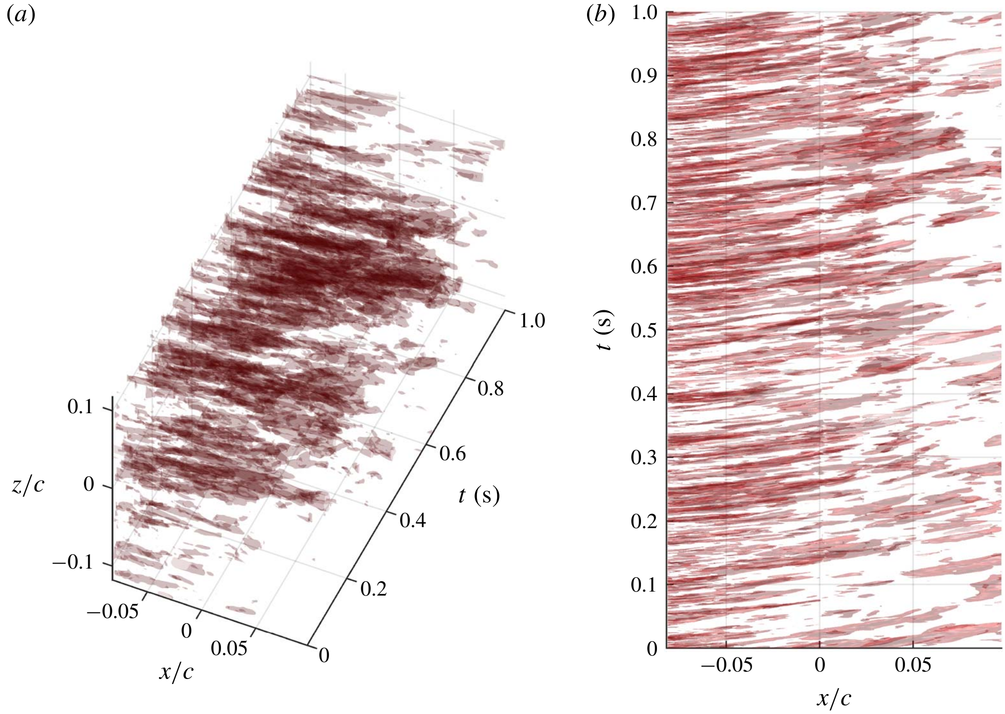

FIGURE 13. (*a*) Isosurfaces of the fluctuating streamwise velocity corresponding to $u/U_\infty = 0.12$. (*b*) The isosurfaces projected onto the *x*–*t* axis to highlight the advection velocity of streaks in the streamwise direction.

The energy content of the first 100 modes is plotted on a semi-logarithmic axis in figure 14. The first mode captures only 2.60 % of the total turbulent kinetic energy content, and the first 100 modes account for 53.7 % of the total energy. This is comparable to the results presented by Duquesne *et al.* (2015), who performed near-wall PIV at the separation front of a turbine diffuser. The amount of energy captured by the top 100 modes in their study ranged from 50 % to 80 % depending on the location of the measurement region. The low energy of the modes is due to presence of small-scale structures and a lack of coherent periodicity as was observed in the PSD.

The first six POD modes are shown in figure 15 and are arranged in descending order of energy content. The vectors in the figure represent the components of the normalized modes while the background contours show the streamwise component of the vectors. Vector arrows are not scaled identically between the subfigures, but the colour map is consistent between them. Mode 1 is symmetric about midspan. It contains a large streamwise fluctuation band with high shear around its border. The fluctuation can be positive or negative and can contribute to high- or low-speed instantaneous velocity, depending on the sign of the temporal coefficient $a_1(t)$. Modes 2–6 reveal similar alternating high- and low-speed streaks that decrease in size with decreasing energy. The streaky pattern of the modes is likely associated with large-scale distortion of the flow field, as the streaks are much larger than those observed in the upstream boundary layer.

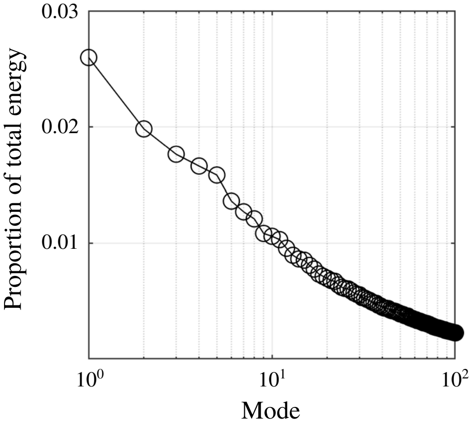

FIGURE 14. The energy content of the first 100 POD modes in the x–z plane of FOV2.

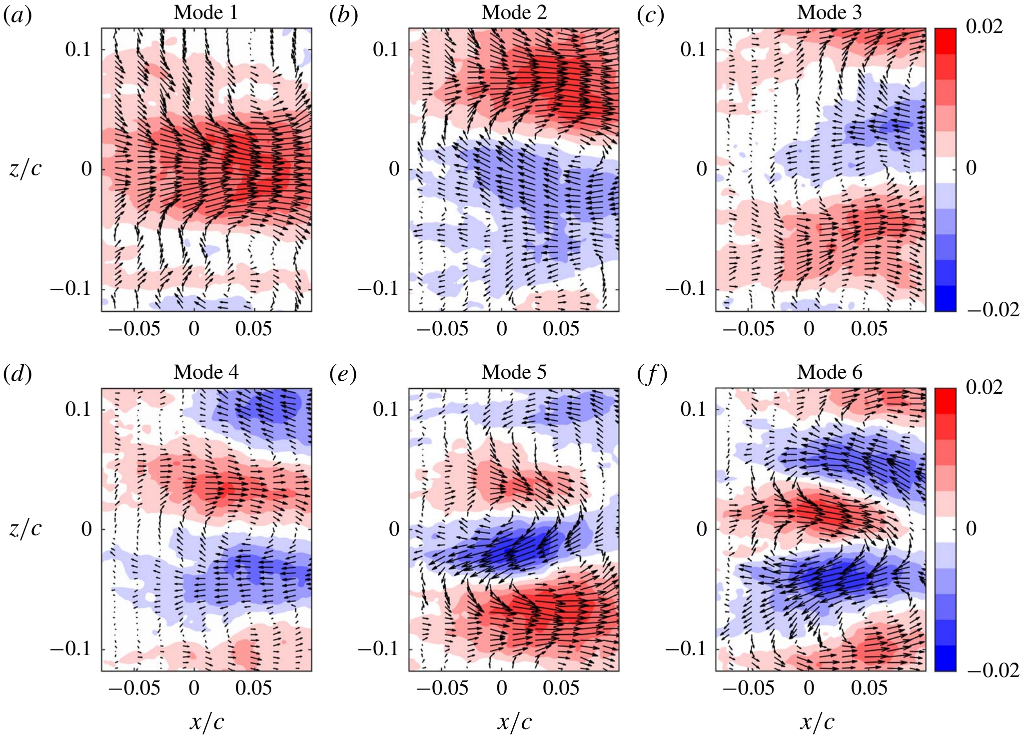

FIGURE 15. The first six POD modes obtained from decomposition of the fluctuating velocity field. Contours of the fluctuating streamwise velocity are shown in the background.

In order to investigate the effect of the first six modes, a reduced-order flow field was constructed by adding the respective mode to the mean velocity field, i.e. $\boldsymbol{U}_r = \langle \boldsymbol{U} \rangle + a_m \boldsymbol{\phi}_m$. The temporal coefficients were chosen based on the root mean square (r.m.s.) value of the temporal coefficients associated with the respective mode, and

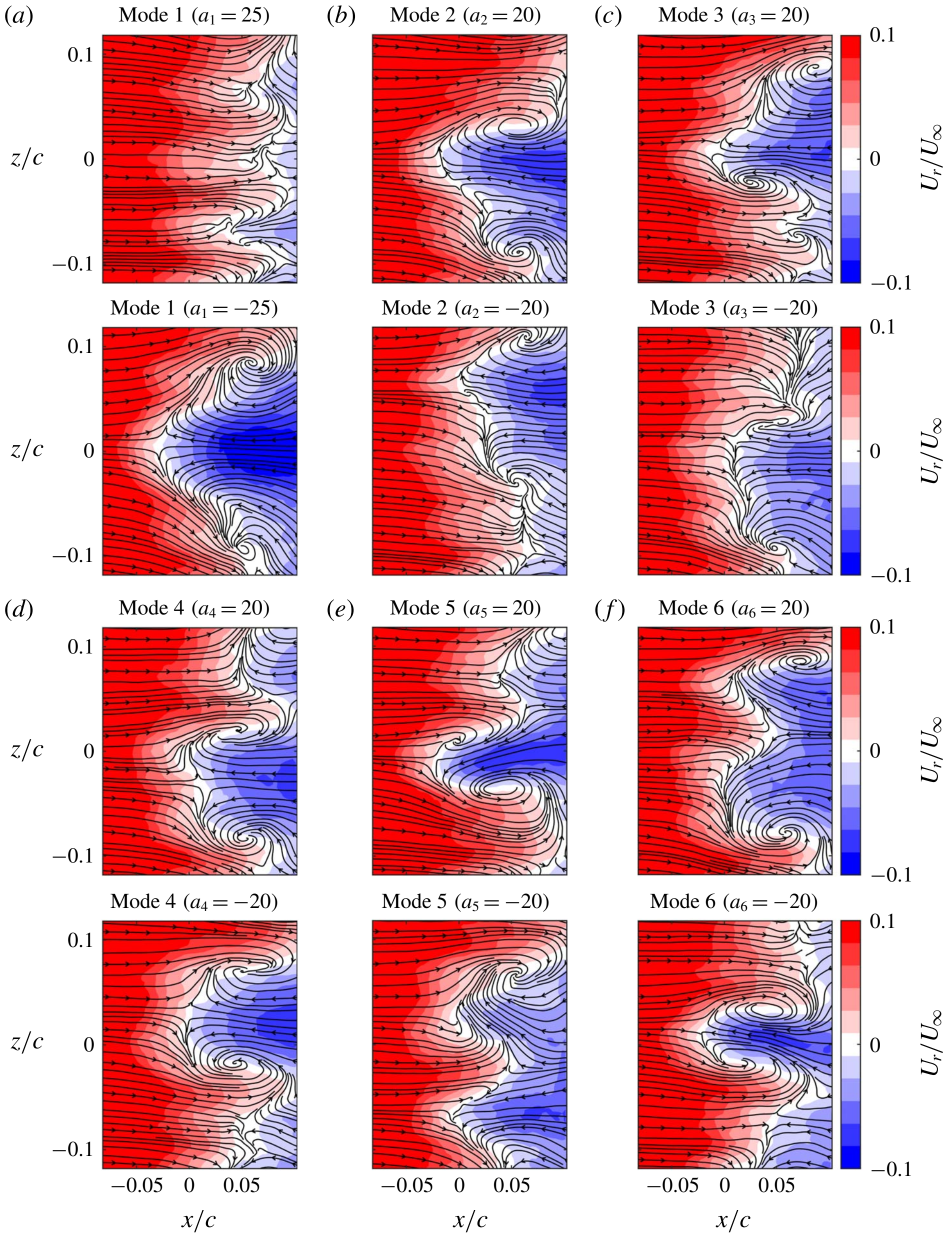

FIGURE 16. Low-order flow fields obtained by superimposing a selected spatial mode with the mean velocity field. The temporal amplitudes a_i are chosen based on the r.m.s. value of the amplitudes associated with the respective mode. The background contours correspond to the normalized streamwise velocity.

both positive and negative coefficients were investigated. Temporal amplitudes of ±25 were used for the investigation of the first spatial mode, and the results are presented in figure 16(a). For the positive amplitude, the stall cell from the mean velocity field is eliminated from the flow pattern. The pair of counter rotating foci and the saddle point are no longer identifiable in the skin friction pattern, and the spanwise variation of the separation front is decreased. The stall cell becomes visible for the negative amplitude case, which is shown in the lower subfigure of figure 16(*a*); the saddle point and foci pair are easily identified here, and a strong backflow is observed near midspan. The flow pattern is also symmetric with respect to midspan. It is clear that mode 1 is related to the alternation between a two-dimensional separation front and a three-dimensional stall cell pattern, as well as the movement of the separation front in the streamwise direction.

Temporal amplitudes of ±20 were used to construct the low-order flow field using modes 2–6 and the results are presented in figure 16(*b–f*). Once again, these values are approximately equal to the associated r.m.s. value of the coefficients within the ensemble. Mode 2 is responsible for shifting the stall cell toward the spanwise side of the airfoil, resulting in an asymmetric stall cell. A large positive amplitude moves the separation front farther downstream for $z/c > 0$ while bringing the separation front upstream for $z/c < 0$, effectively shifting the stall cell in the negative z-direction. A negative amplitude for the second mode has the opposite effect as it moves the stall cell in the positive z-direction. Mode 3 is similar to mode 2 in the sense that it is associated with distorting the stall cell in the spanwise direction. Mode 4 results in a smaller stall cell, shifted in one spanwise direction or the other based on the sign of the mode amplitude. Modes 5 and 6 act as a pair and they strongly control the spanwise distance between the counter-rotating foci. These results indicate that the distortion of the separation front and the movement of the two focus points can be identified as the most energetic motions of the turbulent flow within FOV2.

6. Summary and conclusions

In the present work, two-component PIV was used to study the unsteady organization of a three-dimensional trailing-edge separated flow over an airfoil at $Re_c = 750\,000$. The airfoil was at an angle of attack of 9°, which is located in the nonlinear pre-stall regime of the lift curve. Two fields of view were investigated: one located in a streamwise–wall-normal plane at midspan and another located near and parallel to the airfoil surface at the separation location. The former experiment was used to characterize the turbulent boundary layer profile experiencing an APG, while the latter experiment was used to investigate the topology of the separated flow by analysing the skin-friction patterns.

The velocity profiles, Reynolds stresses, and turbulence transport of the separated boundary layer flow in the streamwise–wall-normal plane at midspan were similar to those reported by other studies of APG-induced flow separation. More specifically, the boundary layers in these flows experience a similar transformation leading up to separation, regardless of the source of the APG or whether the flow is two- or three-dimensional. Another commonality is that the location of peak stress moves away from the wall and broadens as the flow separates, resulting in two distinct regions whose turbulence transport mechanisms are dominated by either ejections or sweeps.

The mean skin-friction lines obtained from near-wall PIV revealed a saddle point near midspan and two counter-rotating foci, each slightly downstream from the saddle point and offset in one spanwise direction or the other. The separation line emanating from the saddle point terminated at the two foci, resembling a stall cell pattern with a spanwise width of $0.17s$. The size of the mean stall cell found here is comparable with results from past investigations. Visualizations of instantaneous skin-friction lines revealed a highly unorganized flow field. Applying a temporal moving-average filter unveiled many saddle points and foci at the separation front. The existence of these separation structures along the separation front resulted in increased Reynolds stresses in this region. The instantaneous saddle points were more or less evenly distributed across the span. Clockwise foci were more densely concentrated towards one spanwise side of the airfoil, and counter-clockwise foci were more concentrated towards the other. The localization of small foci based on their direction of rotation is believed to be responsible for the stall cell pattern in the mean flow field.

The foci within the instantaneous skin-friction lines sometimes appeared in pairs, forming stall cell-like structures that are an order of magnitude smaller than the stall cell depicted in the mean pattern. However, the fact that clockwise and counter-clockwise foci tend to exist on one side of the airfoil or the other indicates that they do not always form in pairs. Instead of one distinct separation line across the span, the instantaneous separation front was made up of many local separation lines formed by the smaller stall cells. The 'instantaneous stall cells' are associated with a strong local streamwise velocity fluctuation between the two foci. The orientation of the instantaneous stall cells depended on the direction of the local flow situated between the foci pair. High-speed streaks from upstream penetrated the separation front to form an instantaneous stall cell with a saddle point on the downstream side of the foci pair, i.e. a 'forward stall cell'. Conversely, strong backflow from the recirculation zone formed instantaneous stall cells with a saddle point on the upstream side of the foci pair – a 'backward stall cell'. In both cases, the tornado-like foci pairs potentially carry the high-momentum fluid in wall-normal directions, causing the high-momentum fluid that formed the instantaneous stall cell to dissipate. These observations were based on the streamwise–spanwise measurement plane that was at a finite wall-normal distance from the airfoil surface. Since the observed stall cells are more than an order of magnitude larger than the gap between the measurement plane and the airfoil surface, and the stall cells consist of foci structures with wall-normal axes, only positional discrepancies are expected with respect to the streamlines at an infinitesimal distance from the airfoil surface.

The formation of forward and backward stall cells was further scrutinized using p.d.f.s of high-speed streak spacing as a function of streamwise distance. If streaks form the instantaneous stall cells, then the size of these stall cells should be comparable to the size of the streaks. This was indeed the case, as the p.d.f.s revealed that the most probable distance between streaks of the same sign was within the range of instantaneous stall cell sizes. Moreover, the distance between streaks increased at streamwise locations further downstream, suggesting that streaks are disappearing as they move into the separation region. This is consistent with the hypothesis that foci pairs eject the high-momentum fluid away from the surface. This was further corroborated by visualizing the advection of high-speed streaks using isosurfaces. The visualization revealed that the concentration of streaky structures was greatly reduced within the separation region.

In agreement with previous studies of shallow stall, the unsteady flow field investigated here was found to be dominated by low-frequency motions ($St < 0.2$). These motions can be associated with the movement of the separation front, as it distorts along its span and undulates in the streamwise direction. Since the separation front is tied to the formation of critical points, these points have been tracked to get a sense of the movement and intermittency of the separation front. The streamwise and spanwise speeds of the critical points in the near-wall plane were roughly $1\,\%$ of U_∞. Their streamwise velocity was smaller but still positive, indicating that the critical points can move both upstream and downstream with a slight tendency towards the downstream direction. The spanwise velocity was negligible, showing that the critical points generally do not exhibit preferential movement in one spanwise direction over the other.

Finally, the most energetic motions in the near-wall plane were investigated using POD. The first mode contained only 2.6 % of the total fluctuation energy, and the first 100 modes captured a cumulative energy of 53.7 %. This is indicative of the complexity of the flow field under investigation, as an accurate low-order representation of the data was not possible. Despite this, the first six modes were investigated in more detail by considering their individual contributions added to the mean flow field. It was shown that these six modes are responsible for distortion and movement of the mean separation front, namely switching between a two- and three-dimensional separation line, moving the mean stall cell in the spanwise directions, or changing the distance between the foci pair. The most energetic motions in the near-wall plane are therefore associated with the movement and distortion of the separation front.

Acknowledgements

We acknowledge the support of the Natural Sciences and Engineering Research Council of Canada (NSERC). We also thank B. Faulkner for manufacturing and assisting with the design of the airfoil and the experimental set-up.

Supplementary movies

Supplementary movies are available at https://doi.org/10.1017/jfm.2020.106.

REFERENCES

ABBOTT, I. H. & VON DOENHOFF, A. E. 1959 *Theory of Wing Sections, including a Summary of Airfoil Data*. Courier Corporation.

ALVING, A. E. & FERNHOLZ, H. H. 1996 Turbulence measurements around a mild separation bubble and downstream of reattachment. *J. Fluid Mech.* **322**, 297–328.

ANGELE, K. P. & MUHAMMAD-KLINGMANN, B. 2006 PIV measurements in a weakly separating and reattaching turbulent boundary layer. *Eur. J. Mech.* (*B/Fluids*) **25** (2), 204–222.

BROEREN, A. P. & BRAGG, M. B. 2001 Spanwise variation in the unsteady stalling flowfields of two-dimensional airfoil models. *AIAA J.* **39** (9), 1641–1651.

COLES, D. & WADCOCK, A. 1979 Flying-hot-wire study of two-dimensional mean flow past an NACA 4412 airfoil at maximum lift. *AIAA J.* **17** (4), 321–329.

DÉLERY, J. 2013 *Three-Dimensional Separated Flow Topology: Critical Points, Separation Lines and Vortical Structures*, pp. 9–14. John Wiley & Sons.

DELL'ORSO, H. & AMITAY, M. 2018 Parametric investigation of stall cell formation on a NACA 0015 airfoil. *AIAA J.* **56**, 1–13.

DENGEL, P. & FERNHOLZ, H. H. 1990 An experimental investigation of an incompressible turbulent boundary layer in the vicinity of separation. *J. Fluid Mech.* **212**, 615–636.

DEPARDON, S., LASSERRE, J. J., BOUEILH, J. C., BRIZZI, L. E. & BORÉE, J. 2005 Skin friction pattern analysis using near-wall PIV. *Exp. Fluids* **39** (5), 805–818.

DUQUESNE, P., MACIEL, Y. & DESCHÊNES, C. 2015 Unsteady flow separation in a turbine diffuser. *Exp. Fluids* **56** (8), 156.

ELYASI, M. & GHAEMI, S. 2019 Experimental investigation of coherent structures of a three-dimensional separated turbulent boundary layer. *J. Fluid Mech.* **859**, 1–32.

GHAEMI, S., RAGNI, D. & SCARANO, F. 2012 PIV-based pressure fluctuations in the turbulent boundary layer. *Exp. Fluids* **53** (6), 1823–1840.

GIBEAU, B. & GHAEMI, S. 2020 The mode B structure of streamwise vortices in the wake of a two-dimensional blunt trailing edge. *J. Fluid Mech.* **884**, A12.

GREGORY, N., QUINCEY, V. G., O'REILLY, C. L. & HALL, D. J. 1971 Progress report on observations of three-dimensional flow patterns obtained during stall development on aerofoils, and on the problem of measuring two-dimensional characteristics. *C.P. No.* 1146. Aeronautical Research Council.

HEINZEL, G., RÜDIGER, A. & SCHILLING, R. 2002 Spectrum and spectral density estimation by the discrete Fourier transform (DFT), including a comprehensive list of window functions and some new at-top windows. *Tech. Rep.* Albert Einstein Institut.

HOLM, R. & GUSTAVSSON, J. 1999 A PIV study of separated flow around a 2D airfoil at high angles of attack in a low speed wind tunnel. *FFA TN*, 52.

JEONG, J. & HUSSAIN, F. 1995 On the identification of a vortex. *J. Fluid Mech.* **285**, 69–94.

JONES, L. E., SANDBERG, R. D. & SANDHAM, N. D. 2008 Direct numerical simulations of forced and unforced separation bubbles on an airfoil at incidence. *J. Fluid Mech.* **602**, 175–207.

LIU, T., WOODIGA, S. & MA, T. 2011 Skin friction topology in a region enclosed by penetrable boundary. *Exp. Fluids* **51** (6), 1549–1562.

LU, F. K. 2010 Surface oil flow visualization. *Eur. Phys. J.* **182** (1), 51–63.

MCCULLOUGH, G. & GAULT, D. 1951 Examples of three representative types of airfoil-section stall at low speed. *NACA Tech. Note* 2502.

MANOLESOS, M., PAPADAKIS, G. & VOUTSINAS, S. G. 2014 Experimental and computational analysis of stall cells on rectangular wings. *Wind Energy* **17** (6), 939–955.

MANOLESOS, M. & VOUTSINAS, S. G. 2014*a* Geometrical characterization of stall cells on rectangular wings. *Wind Energy* **17** (9), 1301–1314.

MANOLESOS, M. & VOUTSINAS, S. G. 2014*b* Study of a stall cell using stereo particle image velocimetry. *Phys. Fluids* **26** (4), 045101.

MEINHART, C. D., WERELEY, S. T. & SANTIAGO, J. G. 2000 A PIV algorithm for estimating time-averaged velocity fields. *Trans. ASME J. Fluids Engng* **122** (2), 285–289.

MOSS, G. F. & MURDIN, P. M. 1970. Two-dimensional low-speed tunnel tests on the NACA 0012 section including measurements made during pitching oscillations at the stall. *C.P. No.* 1145. Aeronautical Research Council.

NA, Y. & MOIN, P. 1998 Direct numerical simulation of a separated turbulent boundary layer. *J. Fluid Mech.* **374**, 379–405.

RAGNI, D. & FERREIRA, C. 2016 Effect of 3D stall-cells on the pressure distribution of a laminar NACA64-418 wing. *Exp. Fluids* **57** (8), 127.

SCARANO, F. & RIETHMULLER, M. L. 1999 Iterative multigrid approach in PIV image processing with discrete window offset. *Exp. Fluids* **26** (6), 513–523.

SCHLICHTING, H. & GERSTEN, K. 2016 *Boundary-Layer Theory*, vol. 474. Springer.

SEARS, W. R. & TELIONIS, D. P. 1975 Boundary-layer separation in unsteady flow. *SIAM J. Appl. Maths* **28** (1), 215–235.

SIMPSON, R. L. 1981 A review of some phenomena in turbulent flow separation. *Trans. ASME J. Fluids Engng* **103** (4), 520–533.

SIMPSON, R. L. 1989 Turbulent boundary-layer separation. *Annu. Rev. Fluid Mech.* **21** (1), 205–232.

SIROVICH, L. 1987 Turbulence and the dynamics of coherent structures. Parts I–III. *Q. Appl. Maths* **45**, 561–590.

SONG, S. & EATON, J. 2002 The effects of wall roughness on the separated flow over a smoothly contoured ramp. *Exp. Fluids* **33** (1), 38–46.

SQUIRE, L. C., MALTBY, R. L., KEATING, R. F. A. & STANBROOK, A. 1962. Flow visualization in wind tunnels using indicators. Part I. The surface oil flow technique. *Tech. Rep.*: AGARDOGRAPH.

SURANA, A., GRUNBERG, O. & HALLER, G. 2006 Exact theory of three-dimensional flow separation. Part 1. Steady separation. *J. Fluid Mech.* **564**, 57–103.

THOMPSON, B. E. & WHITELAW, J. H. 1985 Characteristics of a trailing-edge flow with turbulent boundary-layer separation. *J. Fluid Mech.* **157**, 305–326.

TOBAK, M. & PEAKE, D. J. 1982 Topology of three-dimensional separated flows. *Annu. Rev. Fluid Mech.* **14** (1), 61–85.

WADCOCK, A. J. 1987 Investigation of low-speed turbulent separated flow around airfoils. *NASA Contractor Rep.* 177450.

WEIHS, D. & KATZ, J. 1983 Cellular patterns in poststall flow over unswept wings. *AIAA J.* **21** (12), 1757–1759.

WESTERWEEL, J. & SCARANO, F. 2005 Universal outlier detection for PIV data. *Exp. Fluids* **39** (6), 1096–1100.

WINKELMAN, A. E. & BARLOW, J. B. 1980 Flowfield model for a rectangular planform wing beyond stall. *AIAA J.* **18** (8), 1006–1008.

YON, S. A. & KATZ, J. 1998 Study of the unsteady flow features on a stalled wing. *AIAA J.* **36** (3), 305–312.

ZAMAN, K. B. M. Q., MCKINZIE, D. J. & RUMSEY, C. L. 1989 A natural low-frequency oscillation of the flow over an airfoil near stalling conditions. *J. Fluid Mech.* **202**, 403–442.